Wavelet-based analysis of ground deformation coupling data from satellites (Sentinel-1, SMOS) and from shallow and deep wells in Southwestern France

André Burnol[1*], Hideo Aochi[1], Daniel Raucoules[1], Fernanda M.L. Veloso[1],
Fifamè Koudogbo[2], Pierre Chiquet[3], Christophe Maisons[4]

1. *BRGM, 45000 Orléans, France*
2. *TRE-ALTAMIRA, 31520 Ramonville-St-Agne, France*
3. *TEREGA, 64000 Pau, France*
4. *MAGNITUDE, 04220 Sainte-Tulle, France*

*Corresponding Author. Email: a.burnol@brgm.fr

Abstract:

Acquisitions of the Sentinel-1 satellite are processed and comprehensively analyzed to investigate the ground displacement during a 3-year period above a gas storage site in Southwestern France. Despite quite low vertical displacements (between 4 and 8 mm) compared to the noise level, the local displacements reflects the variations due to charge and discharge during summer and winter periods, respectively. A simplified mechanical model can explain these displacements at both storage sites (Lussagnet and Izaute). However, these low-magnitude ground movements may be also controlled by natural factors, like the temperature or the surface soil moisture (SSM). Using an additive decomposition, we show first that the temperature is only a second order triggering factor compared to the reservoir pressure. Using a wavelet-based analysis, we show there is an uplift in the Lussagnet zone that contrasts both in phase and period with the seasonal deformation due to the gas exploitation and that is linked to the SSM measured by the SMOS satellite. This other displacement is consistent with the water infiltration in the unsaturated zone followed by the expansion of a clay layer. This work provides therefore new insights on the ground deformation using a three-year integrated monitoring of a gas storage site.

Introduction

The Underground Gas Storages (UGS) are designed to address different needs that include establishing a strategic gas reserve, allowing the regulation of the gas supply, meeting seasonal peak heating and electricity demand. Gas is stored from spring to autumn when the demand is lower and withdrawn from October to April, when the demand is higher due to the winter period. In France, another future need is to balance daily load needs arising from the increase of intermittent renewables productions (solar and wind) in the electrical mix. The main issues to be addressed are the geomechanical integrity of both the reservoir and the caprock, the reactivation of existing faults, the leakage through the caprock, fault or any other discontinuity and the movement of the Gas-Water Contact (GWC). UGS development required an appropriate site selection based on subsurface characterization, a suitable performance analysis, based on a fully integrated geological, fluid-dynamic and geo-mechanical approach, and finally a monitoring over the entire life of the storage to satisfy social and environmental concerns and the safety regulations. An integrated monitoring should include at least a network of microseismic sensors, observation wells to follow the reservoir as well as overburden pressures and a technique to measure ground surface displacements over wide areas.

Standard ground surface monitoring techniques provide information on a very limited number of points within an area, both in the cases of geotechnical monitoring (clinometers, extensometers…) or GPS. The idea of a ground displacement monitoring using Differential Synthetic Aperture Radar interferometry (DInSAR) has been intensively developed in the last two decades [1, 2]. Land subsidence related to groundwater extraction or uplift caused by the recharge of aquifers of large cities are some applications of the inSAR technique.

Subsidence in Mexico city center [3, 4], uplift in Brussels city center [5] and both phenomena in Phoenix [6] are just a few recent of many extensively studies using this remote sensing technique. Conversely, the monitoring of gas storage using the DInSAR techniques has received until now far less attention in scientific literature except for some studies dealing with the effects of CO_2 storage [7]. A major limiting factor to this purpose was the non-availability of both spatially and temporally high-resolution SAR dataset. Another limiting factor was the precision of the DInSAR techniques because the deformation linked to gas storage in deep geological layers may be very low in comparison to gas water extraction, typically a few millimeters instead of a few centimeters [6]. Finally, it has been shown that DInSAR techniques are more performant on regular motions than on displacements that have non-linear behavior respect time (i.e with strongly varying rates) as such irregular displacements require finer temporal sampling to be better characterized [8]. This last issue was particularly sensitive with several past space missions for which few acquisitions per year were available (e.g. about 10 per year for Envisat). That was a limitation on the precision on the characterization of an annual cyclic motion. The launch of Sentinel-1A on 3 April 2014, followed by Sentinel-1B on 25 April 2016, changed drastically the availability of Synthetic Aperture Radar (SAR) data by regular acquisition. Sentinel-1 (S-1) constellation has been specifically designed to be suitable for DInSAR applications and ground displacement monitoring. S-1 obtain several frames of SAR data (250 × 250 km^2) along each observation track. Therefore, its imaging parameters, revisit time, spatial resolution, scene coverage, and orbital status are optimized for DInSAR applications [9]. SAR images from the same orbit are acquired every 6 days (combining Sentinel 1A and 1B) over Europe since October 2016.

Due to the potential substantial damage to buildings and infrastructure, the mapping of expansive soils and the quantification of the clay swelling potential is a major concern for natural risk prevention plans. In France, the shrink/swell risk is the second most important cause of financial compensation from insurance companies behind the flood risk. In 2010, based on the spatial distribution of infrastructure damage and the stratigraphy at the resolution of sedimentary basins, the Bureau de Recherches Géologiques et Minières (BRGM) published a predictive 1:50 000 swelling-risk map of France. This map indexed the territory as (i) no, (ii) low, (iii) moderate, or (iv) high risk. In the studied zone in the Aquitaine Basin, there is a low or a moderate swelling risk. At this resolution, the heterogeneity of the mineralogical composition of the sedimentary formations is not taken into account [10-12]. A stratigraphic unit include one or various lithological formations, which may be not considered in the swelling-risk map. Some predictions of the swelling-risk map can be therefore locally inaccurate or even wrong, according to the lithological characteristics of sedimentary formation at the given location. One way to improve this map consists in monitoring soil moisture variations and ground movements by the instrumentation of experimental sites. BRGM has studied three sites in France with different climates (Mormoiron site with a Mediterranean climate and Le Deffend site with a temperate oceanic climate since 2005 and Chaingy site near Orléans since 2015). On each site, capacitive sensors have been installed inside boreholes to track soil moisture variations continuously and at different depths. Extensometers have also been deployed to monitor soil vertical displacements. The first results have confirmed that the seasonal soil moisture variability in the first meters is correlated with the weather conditions and have shown that swelling and settlement ground movements, which occur near the surface, can reach 2 centimeters in only a few months [13]. Another way to improve this swelling-risk map is to use remote sensing satellite or aerial photography. Until now, the DInSAR technique was not operational to map swelling clays, due the non-availability of both spatially and temporally high-resolution and high-quality SAR dataset suitable to the very high variability of such surface deformation phenomena. The question "Can we map swelling clays with remote sensing" asked by Van der Meer in 1999 [14] is still a topical issue.

This work investigates therefore three main questions: (1) Are the displacements measured by the new DInSAR results based on Sentinel-1 acquisitions and the underground gas storage operations at Lussagnet strongly related? ; (2) Can the monitoring based on DInSAR processing be used to monitor the movement of the Gas-Water contact in the reservoir? ; (3) Can the DInSAR processing be used to assess locally the shrink/swell hazard as given by the 1:50 000 geological map? The results section of this paper is organized around these three questions.

Data and Methods

1. Geographical and Geological Setting

The underground gas storage in the studied area is a double storage site lying at the boundaries between both departments "Les Landes" and "Le Gers", situated in the Aquitaine basin in Southwestern France, about 100 km north of the Pyrenees mountain (Fig. 1). The total reservoir structure is an anticline with two culminations, which are only approximately 10 km apart, the Lussagnet reservoir at the west side and the Izaute reservoir at the east side (Fig. 2). The highest point of the top of Lussagnet reservoir is located at a depth of about 545 m below ground level (mbgl) with a thickness of 40 m; the top of Izaute reservoir is at approximatively at 500 mbgl [15]. Both reservoirs are deposited during the Eocene, and are composed of fair consolidated sandstones, called "infra-mollassic sand", with some interlayered claystones [16]. The hydrodynamic parameters of these reservoirs are variable. The total mean porosity of the sandstones varies from 20% to 35%, and their average permeability from 1 to 10 Darcy. The Lussagnet and Izaute gas storage total capacity are respectively equal to 2.9 and 3.0 10^{12} m^3 (referred to normal conditions) and only the working gas, respectively 1.4 and 1.5 10^{12} m^3, is stored and withdrawn during the exploitation cycle. The remaining part, called cushion gas, supplies pressure support and prevents surface installations from excessive water production.

Concerning the surface layer, the shrink/swell hazard with 4 levels (null, low, moderate and high) has already been evaluated in both departments "Les Landes" and "Le Gers" using different criteria, including the surface geological map at the scale 1:50 000 and other geotechnical and mineralogical criteria [17, 18]. In particular, the Tortonien clay surface layer (called "m5" in the 1:50 000 geological map) is characterized by a moderate shrink/swell hazard and the Serravallien sand surface layer (called “m4”) by a low hazard. Just around the gas exploitation wells, there is a moderate shrink/swell hazard at the Lussagnet site and a low hazard at the Izaute site (Fig. 2 and 4).

2. Sentinel-1 DInSAR processing

Interferograms from raw Synthetic Aperture Radar (SAR) data are realized using the descending track 8 (C-band, IW mode, Fig. 1). The deformation rates on 12 days time-span until 1st October 2016 and 6 days thereafter are processed using Persistent Scatterers (PS) and Distributed Scatterers (DS) integrated in the SqueeSAR^{TM} technique [19]. The dataset is composed of 115 raw images from Sentinel-1A and Sentinel-1B (Fig. 3). Two major biases can affect SAR interferograms. Firstly, non-stationary tropospheric SAR signal delay can add an undesired InSAR signal component. This delay can partly – and when the local topography is significant - be correlated to topography, in which case it can be modeled and removed by linear regression with a digital elevation model [20]. Data stacking is also an effective way to reduce the non-topography-related atmospheric noise. Secondly, random temporal changes on the surface of the Earth can reduce the signal to noise ratio (snr), which is characterized through the Interferometric coherence. As a final step, all data are referenced to the PS called C34S9R6 (set to 0 cm/yr), as this PS is steady through time and outside the Tortonian clay surface layer as extracted from 1:50 000 geological map (Fig. 4).

3. Wavelet-based analysis of DInSAR time series

DInSAR processing chains usually compute displacements as the superposition of linear and non-linear terms. In the frequency domain, linear displacements exhibit an infinite period along time and the non-linear component describes the seasonal fluctuations of the displacement, which can exhibit different periods and even changes along time. The continuous wavelet transform (CWT) is especially suited to extract features from low signal-to-noise ratio time-series [21]. CWT expand time-series records into time-frequency space and can therefore find localized intermittent periodicities [22]. The time-series input data for wavelet analysis must be equally spaced in time, i.e. evenly sampled with a fixed time interval. Additionally, two individual CWTs can be combined by using the cross wavelet transform (XWT) tool, if the relationship between two different time series is of interest. XWT is computed by multiplying the CWT of one time-series by the complex conjugate of the CWT of the second time-series. XWT image is the 2-D representation of the absolute value and the phase of the complex number in the time-frequency space. The absolute value of the XWT will be high in the time-frequency areas where both CWTs display high values, so this helps identify time patterns common in the two data sets. The phase of the XWT indicates the time lag between the two time-series. Consequently, this tool is very useful for exploring seasonal patterns which might have a time-lag (shown by the phase of the XWT) between the cause and the effect. XWT tool permits the recognition of common power and relative phase in time-frequency space, along with assessing confidence levels against red noise backgrounds [21].

We describe here a systematic methodology for analysing DInSAR time-series information vs. triggering factors using CWT and XWT for which there are freely available Matlab codes (see the acknowledgement section). First, linear and non-linear components of the displacement time series are separated: the linear component is computed by means of a linear least squares fitting using LINEST Microsoft Excel function and the non-linear component as the difference between the displacement time-series and the previously calculated linear component.

Although SAR satellites have a regular revisit interval (e.g. 35 days for ERS and ENVISAT, 12 days for Sentinel-1A, 6 days for Sentinel-1A/B), some images are usually missing or excluded from processing. Consequently, the time-series data derived from DInSAR processing exhibit usually some gaps (Fig. 3). After the separation between linear and non-linear components, the missing values are interpolated using only the non-linear component, i.e. in our case nine missing values are interpolated using a time interval of 12 days. A second step is the re-sampling of the time-series of potential triggering factors with the same time interval (e.g. bottomhole pressure, rainfall, surface soil moisture, piezometric level). Usually, they present a shorter time sampling (typically 1 day) and consequently, they must be down-sampled to the revisiting time period of the Sentinel-1 (12 days), e.g. for the bottomhole pressure or the piezometric level. However, for some other variables, this re-sampling can be more complex than a simple down-sampling. For the rainfall, a cumulated rainfall during the 12-days period is re-calculated. For the surface soil moisture, an average value for each 12-days Sentinel-1 period has been calculated using the 10-days SMOS Level 3 product as explained in the next section.

4. SMOS Level 3 product (Centre Aval de Traitement des Données)

In situ measurements of soil moisture are limited in their spatial and temporal extent. Satellites provide more extensive spatial coverage and have a temporal resolution ranging from 1 to 35 day(s). We use here the term Surface Soil moisture (SSM) to refer to the volumetric soil moisture in the first few centimetres (0-5 cm) of the soil. The first satellite mission to focus primarily on the collection of soil moisture data was the Soil Moisture Ocean Salinity (SMOS) satellite. SMOS was successfully launched on the 2nd of November 2009 by the

European Space Agency (ESA). SMOS uses microwave radiometry for estimating soil moisture. L-band radiometry is achieved resulting in a ground resolution of 50 km. SMOS Levels L0 to L2 processing products are developed by the ESA. The products are divided in half orbits, from pole to pole, ascending or descending, spanning about 50 minutes of acquisition [23]. Level 3 products are geophysical variables with improved characteristics through temporal resampling or processing. In order to prevent any inconsistency resulting from interpolation over highly heterogeneous surfaces, no spatial averaging is operated in the algorithms. It must also be noted that ascending and descending overpasses are bound to show different values of the retrieved parameters that may not be always comparable and they are thus retrieved separately. The SMOS Level 3 SSM (RE04v300) products were downloaded through the website of the Centre Aval de Traitement des Données SMOS (CATDS, https://www.catds.fr/). The data are presented over the Equal-Area Scalable Earth (EASE grid 2) [24] with a sampling of about 25 km x 25 km (Fig. 1). The performance of each satellite SSM product depends on many factors such as, but not limited to, soil type, climate, presence of noise (Radio Frequency Interference) and land cover. It is therefore difficult to predict the performance of a SSM product over a region, without performing a quality assessment using in situ measurements on that region. A recent published evaluation of the accuracy of SMOS-CATDS products between 1 January 2016 and 30 June 2017 in southwestern France [25, 26] gives an average bias, RMSD (Root Mean Square Difference), ubRMSD (unbiased Root Mean Square Difference) of about -10 vol.%, 12 vol.% and 7 vol.%, respectively. The SMOS-CATDS product thus underestimate the surface soil moisture (with quite high negative bias values) but the ubRMSD of 7% is similar to the best values obtained by other satellites in Southwestern France (about 6%) [25, 26]. The filtered daily global maps are aggregated over different time periods. The SMOS revisit period is 3 days at the equator, so the Earth's surface is covered by SMOS field of view in 3 days and a 3-day global product with a 3-day moving window is provided by CATDS by aggregating the daily global maps. The retrieved SSM data are filtered using the Data Quality Index (DQX) provided in the product (DQX < 0.06 m^3/m^3). The filtering processor is then used over the Level 3 retrievals, to select the best estimation of soil moisture if several retrievals are available for a given day. The CATDS also provides a 10-day product that contains median, minimum and maximum values of soil moisture over 10 days. In this study, the 10-day SMOS-CATDS SSM products for descending overpasses between 18 October 2014 and 26 October 2017 in the grid cell of the studied zone (Fig. 1) are used to calculate the average of the median, minimum and maximum values for each Sentinel-1 period of 12 days.

Results and Discussion

1. SqueeSAR^{TM} time series analysis around gas exploitations wells

To investigate the DInSAR products in both gas exploitation zones, we select eight DInSAR time series in the Lussagnet case using the SqueeSAR^{TM} technique (4 PS and 4 DS) and four-teen DInSAR time profiles in the Izaute case (11 PS and 3 DS) (Fig. 4). Our selection is based mainly on the highest coherence value calculated by SqueeSAR^{TM}. As explained in the method section, we have averaged the non-linear term of all the time-series using a constant time interval of 12 days (Fig. 5). LUG-M8 and IZA-M14 time profiles are the average values of the LOS non-linear displacement in the Lussagnet and Izaute gas exploitation zone, respectively. During the three-year period, the average peak-to-peak LOS displacement amplitude are 5.8 mm ± 1.3 mm in the Lussagnet case and 5.1 mm ± 0.6 mm in the Izaute case (Fig. 6).

Additionally, from the analysis of the root mean square (RMS) of the average of the non-linear component of 10 time-series within a stable area, we assess a RMS of 0.94 mm for the three-year monitoring period (Fig. 5). Less than 1 mm of RMS in a stable area might be considered as a very good score and shows the power of Sentinel-1 DInSAR time-series analyses to detect displacements with magnitudes of as small as a few millimeters, as in the Lussagnet and Izaute cases.

Assuming the expected displacement is mainly in vertical direction, we neglect the contribution of horizontal displacement and transform the displacement from LOS to the vertical using the formula $u_z = LOS/\cos\theta$. Taken into account the local incidence angle of Sentinel-1 sensor (θ = 37.97°), we calculate an average vertical displacement u_z of 7.4 mm ± 1.7 mm and 6.4 mm ± 0.8 mm in the Lussagnet and Izaute case, respectively.

2. Additive decomposition of the DInSAR time series using the deep pressure and the surface temperature variations

Time-series data are often governed by a trend component, a seasonal component and an irregular residual component. There are several different methods available for analyzing those data and some methods are more appropriate than others for different data patterns. Two classical decompositions methods are the additive and the multiplicative decompositions. An additive model is appropriate if the magnitude of the seasonal fluctuations does not vary with the level of time series. Conversely, the multiplicative model is appropriate if the seasonal fluctuations increase or decrease proportionally with increases and decreases in the level of the time series. Concerning the DInSAR time series, an additive form is assumed for the decomposition:

$$TS(t) = T(t) + S(t) + R(t) \qquad (1)$$

This means that after removing both trend part T and seasonal part S, the residual part R should be a stationary process and that’s why the series is called a trend stationary (TS) series. In our decomposition model, the trend part T is supposed to be given by a polynomial trend of degree 2 in time t. The seasonal part itself may be split into different components with an additive form, e.g. one bottomhole pressure component P and one surface temperature component ST:

$$S(t) = \alpha \times P(t) + \beta \times ST(t) \qquad (2)$$

Our method estimates the five coefficients, i.e. both coefficients of trend part (α, β) and three other coefficients of the quadratic trend, by minimizing the residual sum of squares (RSS) for each PS and DS given by SqueeSAR^{TM} technique. We show in Figure 7 the additive decomposition of the time profile of the LOS displacement near the well L1 (DS called BNI5MXO), the sum of the trend and the seasonal part (called “Model”) as well as the comparison of the temperature component of the displacement and the surface temperature. The displacement variation due to the temperature is in anti-phase with the temperature, while the pressure component is in phase with the bottomhole pressure. The key point is that the magnitude of the temperature component of the LOS displacement is at least one order lower than the magnitude of the pressure component (0.3 mm vs. 4 mm, see Fig. 7).

3. Vertical displacement due to reservoir pressure variations

Qualitatively, from the visual comparison between the mean LOS displacement at both sites and the pressure of both storage reservoirs (Fig. 6), one can observe a good correlation between them during the 3-year period. The correlation coefficient is 0.77 in the Lussagnet case and 0.73 in the Izaute case, respectively. It is worth estimating a possible surface deformation (vertical displacement) due to pressure variations in the reservoir and comparing quantitatively with the DInSAR surface observations. In order to know briefly its amplitude, we adopt a linear elastic theory from [27] and [28]. The vertical displacement (u_z) is expressed by an integral equation over the volume where pore pressure changes (Fig. 8). For a uniform distribution of pressure change (ΔP) within a horizontally laid disk-shape reservoir (radius of R_0 and a depth between h_b and h_t) in a homogeneous, semi-infinite elastic medium, we have the integral equation as follows:

$$u_z(r, z = 0) = -(1 - 2\nu)\frac{\alpha}{\mu}\Delta P \int_{h_1}^{h_2} \int_0^{R_0} R \int_0^{\infty} \xi J_0(R\xi) J_0(r\xi) e^{-h\xi} d\xi dR dh \qquad (3)$$

where cylindrical coordinate (r, z) is taken (Fig. 8A), and $J_0(x)$ is the Bessel function of the first kind for integer order 0. For taking into account of realistic reservoir geometry, we subdivide it by many point sources in order to conserve the reservoir volume and we take a summation over all the contribution of each part of the reservoir. The assumed model parameters are summarized in Table 1.

This is a phenomenological, namely kinematic, expression without solving hydrogeological or geomechanical system of the reservoir. From the geological map (Fig. 2), we estimate the extension of the reservoir as 5.4 km^2 for Lussagnet and 13.1 km^2 for Izaute, respectively (Fig. 8A). The gas is stored at the top of the reservoir such that the aquifer level is lowered. Schematically we simplify this by a vertical cylindrical reservoir in which the injected gas pushes down the native water. The modeling geometry is therefore simply vertical so that the deformation pattern calculated through Equation (3) concentrates around the reservoir surface (Fig. 8B). From this estimation, the vertical displacement on the ground surface arrives at 8 mm and 4 mm for Lussagnet and Izaute, respectively (Fig. 8C). The deformation pattern is quite independent, meaning that the deformation amplitude is close to zero half way in-between the two reservoirs. The amplitude is consistent with the DInSAR measurements in the Lussagnet case (7.4 ± 1.7 mm), but lower than the DInSAR measurements in the Izaute case (6.4 ± 0.8 mm) (see previous section). As it is clear from Equation (1), the amplitude of deformation depends strongly on the material constants (ν, μ, α) given in Table 1. In the case where these three parameters vary with ±10%, u_z changes between +41% and -30%. In the Izaute case, this gives an upper bound of the simulated vertical displacement of 5.6 mm, which is consistent with the DInSAR measurement (6.4 ± 0.8 mm). It can also be noted that , a smaller reservoir geometry shall lead to a larger amplitude at the center of the reservoir. However, this first calculation allows briefly estimating the range of possible deformation of the ground surface under simple hypotheses and the associated uncertainties, showing that a vertical displacement amplitude between 4 mm and 8 mm is possible and that the amplitude is higher in the Lussagnet case than in the Izaute case, as observed by DInSAR processing.

Nonetheless, despite a general consistency, some significant features in the Lussagnet case are difficult to explain only by the reservoir pressure variations. In 2015, the maximum of pressure change in the reservoir was 24.6 bar with a minimum of LOS displacement of 4.1 mm, whereas in 2016 (Fig. 6A) the maximum of LOS displacement was 7.3 mm with a minimum of pressure change of 18.7 bar. More particularly, there is an uplift of about 1.2 mm during a 2-month period during the first semester of year 2016, while there is a decrease of the reservoir pressure of 6 bar during the same period (Fig. 6A). We do not observe other significant differences between the LOS displacement and the reservoir pressure for other sub-periods in the Lussagnet case and in the Izaute case (Fig. 6B). Our hypothesis is that this significant difference during this short period might be due to the clay swelling in the Lussagnet zone, as supported by the current swelling risk map (Fig. 2 and 4A,B).

According to our simplified model, the monitoring wells in both sites are outside the domain influenced by the gas injection, i.e. the vertical displacement amplitude due to the gas injection at these monitoring wells is less than 1.25 mm (corresponding to a maximum peak-to-peak less than 2.5 mm) (Fig. 8B). Therefore, it is sound to investigate the mean LOS displacement at the monitoring wells around both gas exploitation zones, in order to decouple the vertical displacement due to the gas injection from other potential phenomena (e.g. clay swelling). First, we focus our attention on the comparison between LOS displacements at the aquifer monitoring wells around the gas bubble and piezometric levels during the first 2 years and half (Fig. 9 and 10). In contrast to the result in the gas exploitation zone itself, there is no obvious correlation between these two time series and the signal-to-noise ratio of the LOS time series is low. To investigate further these LOS displacements, we use wavelet-based tools which have demonstrated their usefulness in this context of seasonal variations to extract features from low signal-to-noise ratio time-series (see the method section). The proposed methodology is to study the time-frequency relationships between the surface displacements measured by DInSAR and three potential natural triggering factors: (1) the cumulated rainfall acquired by the Mont-de-Marsan Weather Station (Fig. 1), (2) the surface soil moisture acquired by the SMOS satellite in a 25km grid cell around the studied area (Fig. 1), (3) the shallow phreatic groundwater piezometric level measured at Latrille (Fig. 2).

4. Wavelet-based analysis of DInSAR time series around Lussagnet monitoring wells (L2, L3, L4)

The continuous wavelet transform (CWT) of the LOS time series at the three monitoring wells (L2, L3, L4) are compared to the CWT of three natural triggering factors time series. From the analysis of the CWT of the rainfall time series (Fig. 11), we can observe two cycles (8-month and 4-month) during the year 2 in addition to the 1-year cycle. The CWT of the Surface Soil Moisture is similar to the rainfall CWT for the 4-month period, with a higher power for the 1-year cycle but with less power for the 8-month period. From the analysis of the continuous wavelet power of the Latrille piezometric level, we can observe only the 1-year cycle. From the analysis of the CWT of the LOS time-series (Fig. 12), some power signals with a significant level against red noise can be recognized with a period of 4 to 8 months at L3 and L2 and with a period of 4 months at L4 during the year 2.

We use now the tool XWT between the LOS displacements and natural triggering factors. From the cross analysis with the rainfall, we see a high common power with a period of 4 months and 8 months and with a significant level against red noise with the LOS displacement at L3 and L2 during the first semester of year 2 (between December 2015 and April 2016, see Fig. 13B). During this episode, the rainfall is in phase with the LOS displacement at L3 (arrow pointing right) and is leading the LOS displacement at L2 (arrow pointing down). A similar high common power with a period of 4 months can be recognized for the LOS displacement at L4. Using the Surface Soil Moisture instead of the rainfall (Fig. 13D-F), the cross analysis give a similar high common power with the period of 4 months at L3 and L2 with a significant level against red noise.

In conclusion, XWT reveals the role of one rainfall episode between December 2015 and April 2016 on the surface displacement. We will therefore compare in the next section the time series of the LOS displacements in the Lussagnet zone during this 6-month episode.

5. Modeling of the LOS displacements in the Lussagnet zone between December 2015 and April 2016

From the analysis of the CWT of the LOS time-series, we can observe a clear 1-year cycle (period) for the Lussagnet exploitation zone (LUG-M8) during the whole monitoring three-year period (Fig. 14A). Between December 2015 and April 2016, a common power with the period of 4 months can be recognized (first semester of year 2 in Fig. 14A) but with a much lower magnitude than for the monitoring wells (L3, L2 and L4) (see previous section). From the cross wavelet transform (XWT) with the bottomhole pressure at L1 (Fig. 14B), the visual observation shown in Fig. 6 of a strong in-phase relation between both time series is confirmed for the one-year cycle (arrows pointing right). From the cross analysis with the rainfall, there is a common power with a period of 4 months during the first semester of year 2 (Fig. 14C) and the rainfall is leading the LOS displacement LUG-M8 (arrows pointing down).

The times series of the LOS displacement at the monitoring wells L2, L3 and L4 are compared with the rainfall and the Surface Soil Moisture (SSM) during the time interval between December 2015 and April 2016 (Fig. 15). The amplitude of the LOS displacement increase is 4.4 mm and 5.4 mm for L2 and L4, respectively. The amplitude of the LOS displacement decrease is about 5 mm for L3. The LOS displacement at L3 is in phase with the rainfall and the Surface Soil Moisture and is leading the LOS displacement at L2 and L4. This time lag may be due to the infiltration time of water from the surface to the clay layer in the unsaturated zone. To confirm this hypothesis, we extract from the BRGM subsurface database called "Banque de données du Sous-Sol" (BSS) the available geological logs near the Lussagnet wells. According to the BSS, the clay layer is near the surface at L3 and is at the same depth (3-m) at L2 and near the gas exploitation wells (LUG-M8) (Fig. 16). All these results are consistent with the hypothesis of a vertical component of the ground due to the clay swelling in the Lussagnet gas exploitation zone at the beginning of the year 2016, as speculated previously. In order to estimate the LOS displacement around the gas exploitation wells at the DS called BKB8Z5Y (near L1), we use first a sinusoidal regression model using a one-year period to simulate the displacement due to the pression change, the result is a sinusoidal function F:

$$F(t) = A_{max} \cos\big((t+\varphi) \times 2\pi/T\big) \qquad (4)$$

Where t is the time in days (relative to 18 October 2014), A_{max} the amplitude of 2 ± 0.32 mm, φ the phase delay of 32 days days and T the period of 365 days. We add to this sinusoidal model the LOS displacement at L2, supposing that the vertical displacement due to the clay swelling is the same at both locations because of the same depth of the clay layer:

$$M(t) = F(t) + L2(t) \tag{5}$$

Indeed, this new model M(t) fits quite well the displacement for the DS called BKB8Z5Y (near L1) between December 2015 and April 2016 (Fig. 17).

In conclusion, the combination of a LOS displacement due to the pressure change and a displacement due to the swelling of a 3-m depth clay layer fits well the data around the Lussagnet gas exploitation zone between December 2015 and April 2016. The LOS amplitude of the swelling/shrinking in the Lussagnet zone during this rainfall episode is about 5 mm and the time interval of the cycle swelling/shrinking is about 4 months. We use in the next section the same wavelet-based method to analyze the LOS displacements in the Izaute zone to support these conclusions.

6. Wavelet-based analysis of DInSAR time series around Izaute monitoring wells (I2, I3, I4, I5)

From the analysis of the CWT of the InSAR time-series, we can observe a clear 1-year cycle (12-month period) for the Izaute exploitation zone (IZA-M14) during the whole monitoring three-year period (Fig. 18C). Additionally, some power signals during the first semester of year 2 (between December 2015 and April 2016) with a significant level against red noise can be recognized with a period of 4 months and 8 months at I4 (Fig. 18A) and with a period of 4 months at I2 (Fig. 18B). From the cross analysis with the rainfall, we see a high common power during the first semester of year 2 with a period of 4 months and 8 months and with a significant level against red noise with the LOS displacement at I4 and at I2 (Fig. 18). During this episode and this 4-month period, the rainfall is leading the LOS displacement at I4 by about one month (arrow pointing straight down, Fig. 18D) and is in anti-phase with the LOS displacement at I2 (arrow pointing left, Fig. 18E). Interestingly, the XWT reveals that the rainfall is also leading during this episode the LOS displacement near the gas exploitations wells (IZA-M14) but with a very low magnitude compared to the Lussagnet case (Fig. 18F). The presence of small-scale lenses of clays in the Izaute exploitation zone (not indicated by the 1:50 000 geological map) may explain this last result.

In conclusion, XWT reveals the role of this rainfall episode between December 2015 and April 2016 for the LOS displacement around the monitoring wells in the Izaute zone. In a similar way to the Lussagnet case, we compare in the next section the time series of the LOS displacements near the Izaute monitoring wells during this rainfall episode.

7. LOS displacements in the Izaute zone between December 2015 and April 2016

The times series of the LOS displacement at the monitoring wells I5, I4, I2 and I3 are compared with the rainfall and the Surface Soil Moisture (SSM) during the time interval between December 2015 and April 2016 (Fig. 19). The LOS displacement at I5 is leading the displacement at I4, which is leading the LOS displacement at I2. There is no significant LOS displacement at I3. As indicated by the phase of the XWT (see previous section), the rainfall is leading the LOS displacement at I4 by about one month and the LOS displacement at I2 by about two months. Interestingly, the LOS displacement at I4 displacement is very similar in phase with the LOS displacement at L2, with a leading phase of L2. These results are consistent with the depth of the clay layer which is 3 m at L2, 4 m at I4 and 5 m at I2 given by the geological logs from the BRGM subsurface database (Fig. 20).

8. A new method coupling satellites acquisitions (Sentinel-1 and SMOS) and the BSS database to improve the global French shrink/swell hazard map

As shown in the previous sections, the most complex task is to extract the signal linked to the clay swelling from the noise in the DInSAR results (typically 5 mm in this work). Locating the areas of low-magnitude soil vertical expansion would be useful for predicting areas with a high risk of shrinking in the event of a long drought (e.g. the drought episode between 1989 and 1991 in Southwestern France). The two limiting factors to this purpose is the quality of the SAR dataset (PS and DS) and the availability of data from the BSS subsurface database in the vicinity of the scatterers (PS and DS). In presence of buildings or of a dense vegetation, the quality of the scatterers may be indeed not sufficient to detect these low-magnitude vertical displacements. We show here first that the wavelet-based analysis is a powerful tool to quantify the correlation (amplitude and phase) between the LOS displacement and the surface soil moisture acquired using both satellites (Sentinel-1 and SMOS). As a second step, the geological logs extracted from the BSS database spatially close to the dataset of scatterers (PS or DS) may be used to test the phase consistency. The method described in this work coupling both satellite acquisitions (Sentinel-1 and SMOS) and the BSS database may be generalized using the global SAR dataset (PS and DS) in metropolitan France to improve the global French shrink/swell hazard map.

Conclusion:

By combining Sentinel-1 interferometric products and observations from a network of shallow and deep wells, we performed a first integrated monitoring of the underground gas storage Lussagnet-Izaute, between October 2014 and October 2017. This integrated monitoring, along with the high temporal resolution of the Sentinel-1 interferograms (12 days), allowed us to estimate a cyclic deformation due to gas injection and withdrawal cycles during the summer and winter periods. Using a sinusoidal regression with a one-year period, we show that the amplitude of the seasonal displacement around the Lussagnet gas exploitation wells is between 4 and 5 mm. A comprehensive analysis of the ground deformation at the Lussagnet site using the monitoring wells and the comparison with the Izaute site suggests also the presence of a transient surface deformation that contrasts both in phase and period with the cyclic deformation due to gas exploitation, but with a similar amplitude (about 5 mm). This last result is consistent with the swelling of the clay layer described in the geological logs extracted from the BRGM subsurface database (BSS). In these terms, the measurement of the surface motion with the high spatio-temporal resolution of the satellite Sentinel-1 appears as an improvement for our understanding of the combination of two different processes driving the ground surface displacement, i.e. the reservoir pressure variation and the swelling/shrinking of a surface clay layer. This 3-year monitoring coupling satellites acquisitions and underground wells data is a first step and this integrated monitoring will benefit in the future from the aggregation of heterogeneous data over longer time periods.

Acknowledgments

ENTREPOSE-GEOSTOCK is the sponsor of the project Web-RDS funded by the program CITEPH (Collaborative Technological Innovation in Energy Domains, http://www.citeph.fr/en/). The reservoir data was provided by the gas storage operator TEREGA (https://www.terega.fr/en/). Acquisitions of Sentinel-1 satellite were provided by the European Space Agency (ESA, https://sentinel.esa.int/web/sentinel/sentinel-data-access) and Soil moisture data of SMOS satellite by the French ground segment for the Level 3 data (CATDS, https://www.catds.fr/). The MATLAB wavelet toolbox is provided by A. Grinsted (http://www.glaciology.net/wavelet-coherence) and the wavelet software by C. Torrence and G. Compo (http://paos.colorado.edu/research/wavelets/).

Authors contributions:

A.B wrote the main manuscript, prepared the figures 1-7 and 9-20, performed the SMOS data and the BSS database processing, the wavelet-based analysis and the overall interpretation. H.A performed the geomechanical modeling, contributed to the text writing and prepared the figure 8 and the table 1. F.V performed the geological data processing. F.K performed the S1 data processing, performed the additive decomposition of the S1 data. D.R contributed to the interpretation of S1 data and to the text writing. P.C performed the gas storage exploitation data processing. C.M conceived and supervised the CITEPH Web-RDS project and contributed to the overall interpretation. All authors reviewed the manuscript.

Competing Financial Interests

The Authors declare that they have no competing financial interests.

References

1. Massonnet, D. & Feigl, K. L. Radar interferometry and its application to changes in the Earth's surface. *Rev. Geophys.* **36**, 441-500 (1998).
2. Hanssen, R. F. in *Radar interferometry: data interpretation and error analysis* (Springer Science & Business Media, 2001).
3. Sowter, A. *et al*. Mexico City land subsidence in 2014–2015 with Sentinel-1 IW TOPS: Results using the Intermittent SBAS (ISBAS) technique. *International Journal of Applied Earth Observation and Geoinformation* **52**, 230-242 (2016).
4. Strozzi, T. &Wegmuller, U. *Land subsidence in Mexico City mapped by ERS differential SAR interferometry* (Geoscience and Remote Sensing Symposium, 1999. IGARSS'99 Proceedings. IEEE 1999 International Ser. 4, IEEE, 1999).
5. Declercq, P. *et al*. A Study of Ground Movements in Brussels (Belgium) Monitored by Persistent Scatterer Interferometry over a 25-Year Period. *Geosciences* **7**, 115 (2017).
6. Miller, M. M. & Manoochehr, S. Spatiotemporal characterization of land subsidence and uplift in Phoenix using InSAR time series and wavelet transforms. *J. Geophys. Res. Solid Earth* **120**, 5822-5842 (2015).
7. Rohmer, J. & Raucoules, D. On the applicability of Persistent Scatterers Interferometry (PSI) analysis for long term CO2 storage monitoring. *Engineering Geology* **147-148**, 137-148 (2012).
8. Raucoules, D. *et al*. Validation and intercomparison of Persistent Scatterers Interferometry: PSIC4 project results. *J. Appl. Geophys.* **68**, 335-347 (2009).
9. Salvi, S. *et al*. The Sentinel-1 mission for the improvement of the scientific understanding and the operational monitoring of the seismic cycle. *Remote Sensing of Environment* **120**, 164-174 (2012).
10. Dufréchou, G., Hohmann, A., Bourguignon, A. & Grandjean, G. Targeting and mapping expansive soils (Loiret, France): geometrical analysis of laboratory soil spectra in the short-wave infrared domain (1100–2500 nm). *Bulletin de la Société géologique de France* **187**, 169-181 (2016).
11. Bourguignon, A., Delpont, G., Chevrel, S. & Chabrillat, S. Detection and mapping of shrink-swell clays in SW France, using ASTER imagery. *Geological Society, London, Special Publications* **283**, 117 (2007).
12. Truche, C. *Characterization and quantification of clay minerals in expansive soils by infrared spectrometry on laboratory and field scales,* PhD dissertation (Université Paul Sabatier - Toulouse III, 2010).
13. Vincent, M., Le Roy, S., Dubus, I. & Surdyk, N. Experimental monitoring of water content and vertical displacements in clayey soils exposed to shrinking and swelling. *Revue Française de Géotechnique*, 45-58 (2007).
14. van der Meer, F. Can we map swelling clays with remote sensing? *International Journal of Applied Earth Observation and Geoinformation* **1**, 27-35 (1999).
15. DOUEZ, O. *Response of a multi-layered aquifer system to the paleoclimatic variations and the anthropic pressure (approach to coupled hydrodynamical, thermal and geochemical modelling),* PhD dissertation (Université Michel de Montaigne, Bordeaux, 2007).
16. Cavelier, C., Friès, G., Lagarigue, J. L. & Capdeville, J. P. Early Cenozoic prograding sedimentation in southern Aquitaine: a model. *Géologie de la France* **4**, 69-79 (1997).
17. Norie, A., Capdeville, J. P. & Vincent, M. Cartographie de l'aléa retrait-gonflement des sols argileux dans le département du Gers. **BRGM/RP-51251-FR** (2001).
18. Karnay, G. Cartographie de l'aléa retrait-gonflement des sols argileux dans le département des Landes. **BRGM/RP-56583-FR** (2008).
19. Ferretti, A. *et al*. A new algorithm for processing interferometric data-stacks: SqueeSAR. *IEEE Trans. Geosci. Remote Sens.* **49**, 3460-3470 (2011).
20. Bekaert, D., Walters, R., Wright, T., Hooper, A. & Parker, D. Statistical comparison of InSAR tropospheric correction techniques. *Remote Sens. Environ.* **170**, 40-47 (2015).
21. Torrence, C. & Compo, G. P. A practical guide to wavelet analysis. *Bull. Am. Meteorol. Soc.* **79**, 61-78 (1998).

22. Grinsted, A., Moore, J. C. & Jevrejeva, S. Application of the cross wavelet transform and wavelet coherence to geophysical time series. *Nonlinear processes in geophysics* **11**, 561-566 (2004).
23. Kerr, Y. H. *et al*. The SMOS Soil Moisture Retrieval Algorithm. *IEEE Transactions on Geoscience and Remote Sensing* **50**, 1384-1403 (2012).
24. Brodzik, M. J., Billingsley, B., Haran, T., Raup, B. & Savoie, M. H. EASE-Grid 2.0: Incremental but Significant Improvements for Earth-Gridded Data Sets. *ISPRS International Journal of Geo-Information* **1** (2012).
25. Al Bitar, A. *et al*. The global SMOS Level 3 daily soil moisture and brightness temperature maps. *Earth System Science Data* **9**, 293-315 (2017).
26. El Hajj, M. *et al*. Evaluation of SMOS, SMAP, ASCAT and Sentinel-1 Soil Moisture Products at Sites in Southwestern France. *Remote Sensing* **10** (2018).
27. Geertsma, J. Land subsidence above compacting oil and gas reservoirs. *J. Pet. Technol.* **25**, 734-744 (1973).
28. Segall, P. Induced stresses due to fluid extraction from axisymmetric reservoirs. *Pure Appl. Geophys.* **139**, 535-560 (1992).

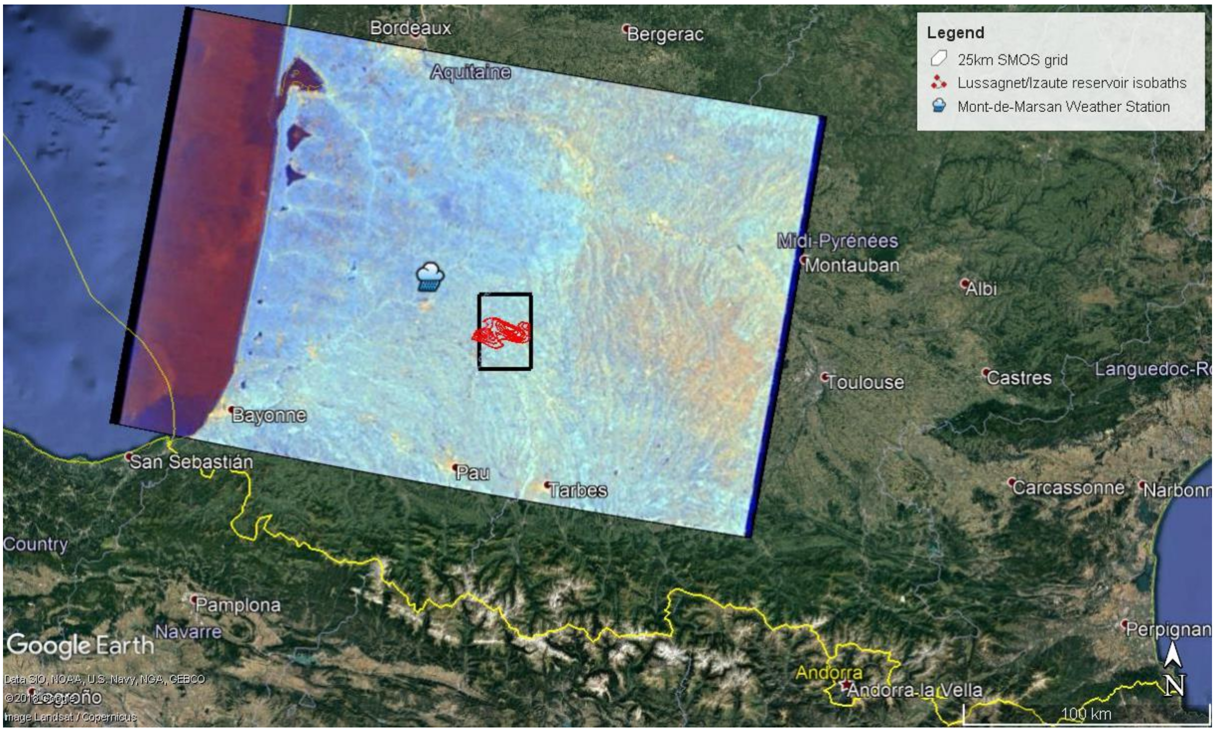

Figure 1: Location map of Aquitaine Basin (South West France) showing a Sentinel-1 image acquisition (2016/01/05), the Mont-de-Marsan weather station, the Lussagnet/Izaute reservoir isobaths (red lines) and a 25 km cell of the EASE equal-area grid used by the SMOS satellite (black square).

Figure 2: Location map of the studied zone between the river L'Adour at the West and La Midouze at the East with the Lussagnet storage reservoir isobaths between 450 m/NGF and 875 m/NGF (turquoise blue). On the western edge is located the Lussagnet gas exploitation wells (around L1 red circle) and on the eastern edge the Izaute gas exploitation wells (around I1). The monitoring wells are shown by blue circles, the Latrille piezometric borehole by the blue placemark and the 25 km SMOS grid cell by both black vertical lines. Also shown is the medium shrink/swell hazard (orange domain) based on the 1:50 000 geological map.

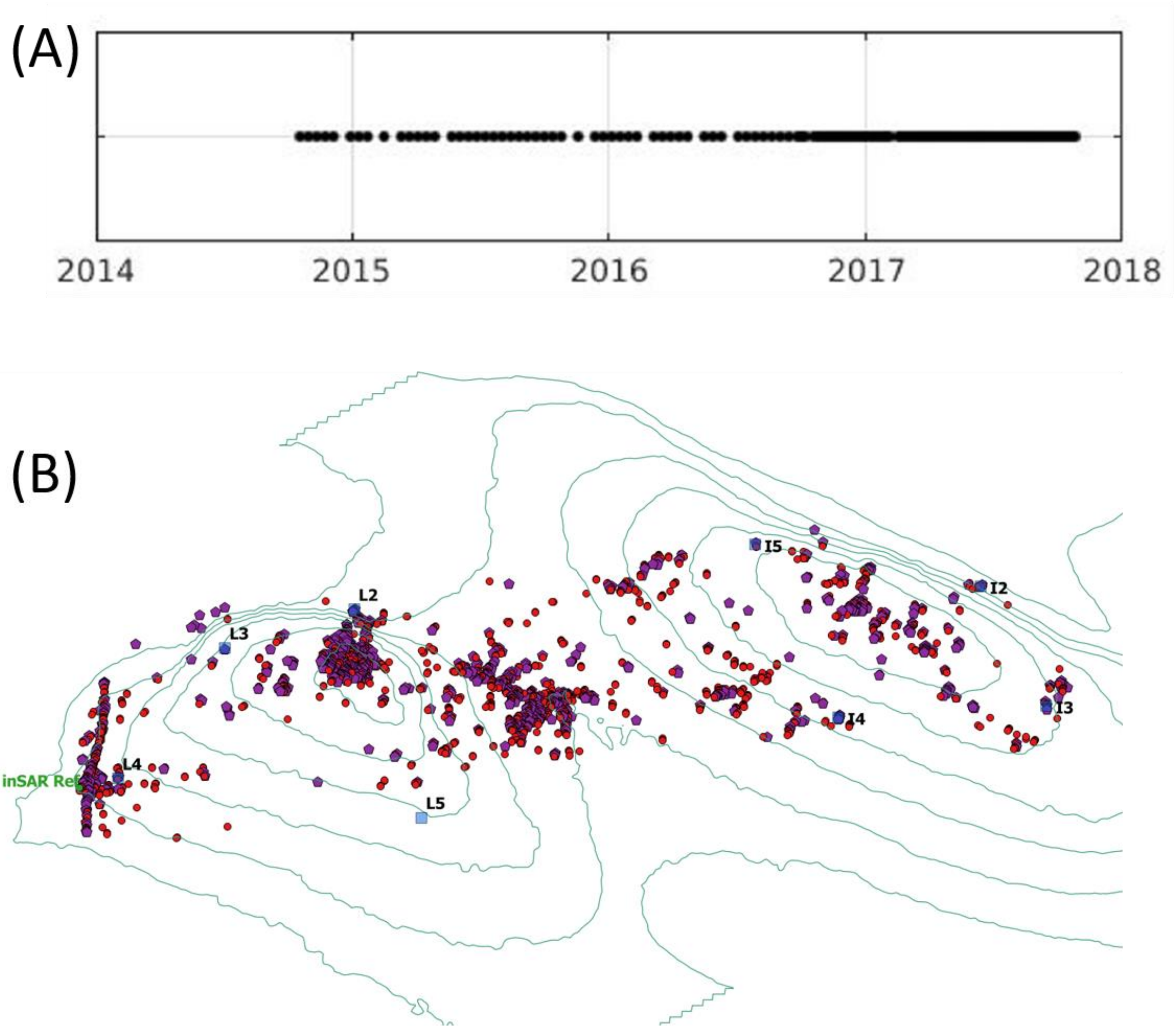

Figure 3: Spatio-temporal distribution of Sentinel-1 acquisitions using SqueeSARTM method. (A) Temporal distribution of the 115 scenes every 12 days during 2014/10/18-2016/10/1 using Sentinel-1A and every 6 days during 2016/10/1-2017/10/26 using Sentinel-1A/1B. (B) Horizontal map of 1931 measurement points including 1303 Persistent Scatterer PS (red circle) and 628 Distributed Scatterer DS (pink pentagon) located within the reservoir isobaths (turquoise blue). Also shown are the relative locations of the monitoring wells (blue squares) and the reference point used for the interferometric phase unwrapping (green circle called “inSAR Ref”).

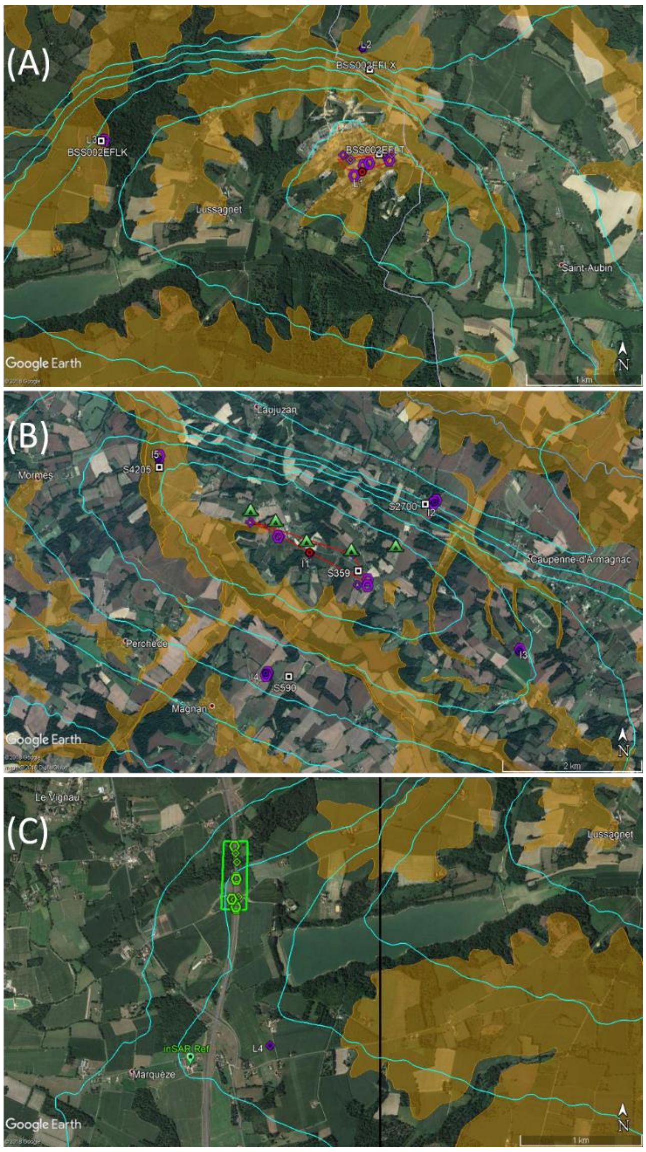

Figure 4: Detailed map of three sub-zones in the studied area. (A) Lussagnet exploitation zone (red pentagon) with four PS (purple diamond) and four DS (purple hexagon) inside the 450 m/NGF isobath and two monitoring wells (L2, L3). (B) Izaute exploitation zone around (red triangle) with five Corner Reflectors (green triangle), six other PS (purple losange) and three DS (purple hexagon) inside the 450 m/NGF isobath and four monitoring wells (I2, I3, I4, I5). (C) Western edge of the studied zone with the reference zone (green) including 10 measurement points around the 790 m/NGF isobath with 4 PS (green diamond) and 6 DS (green hexagon), the reference point used for the interferometric phase unwrapping (green placemark “inSAR Ref”) and one monitoring well (L4). Also shown are the locations of the geological logs (white squares) extracted from the BRGM subsurface database and the medium shrink/swell hazard (orange domain) based on the 1:50 000 geological map.

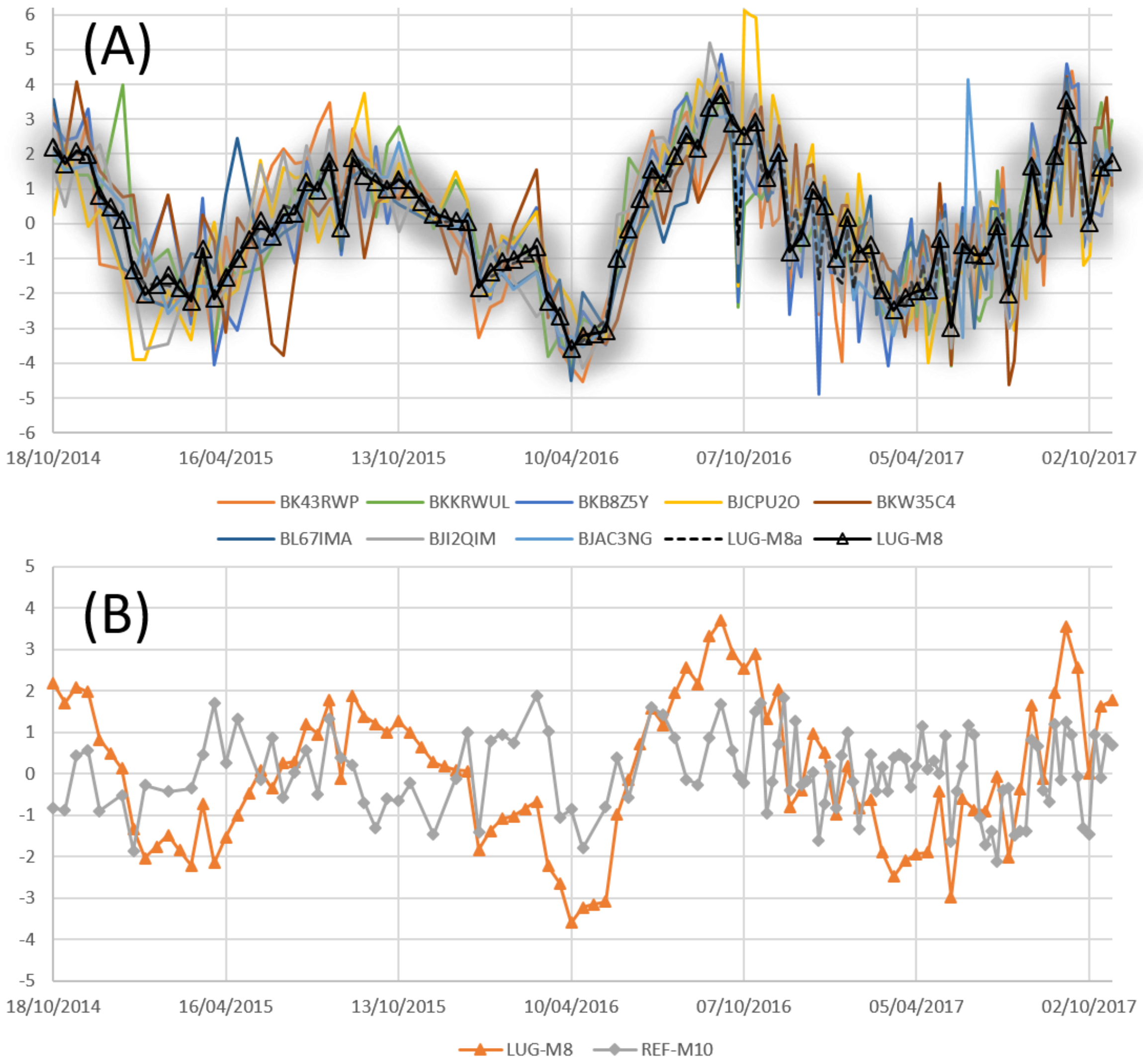

Figure 5: (A) Time profiles of eight Line of Sight (LOS) displacements (4 PS and 4 DS) around the Lussagnet exploitation wells and the mean value (called LUG-M8a) and the mean time value with a constant time sampling of 12 days (called LUG-M8). (B) Comparison of LUG-M8 and the LOS displacement (called REF-M10) in the reference zone away from cyclic seasonal deformation zones.

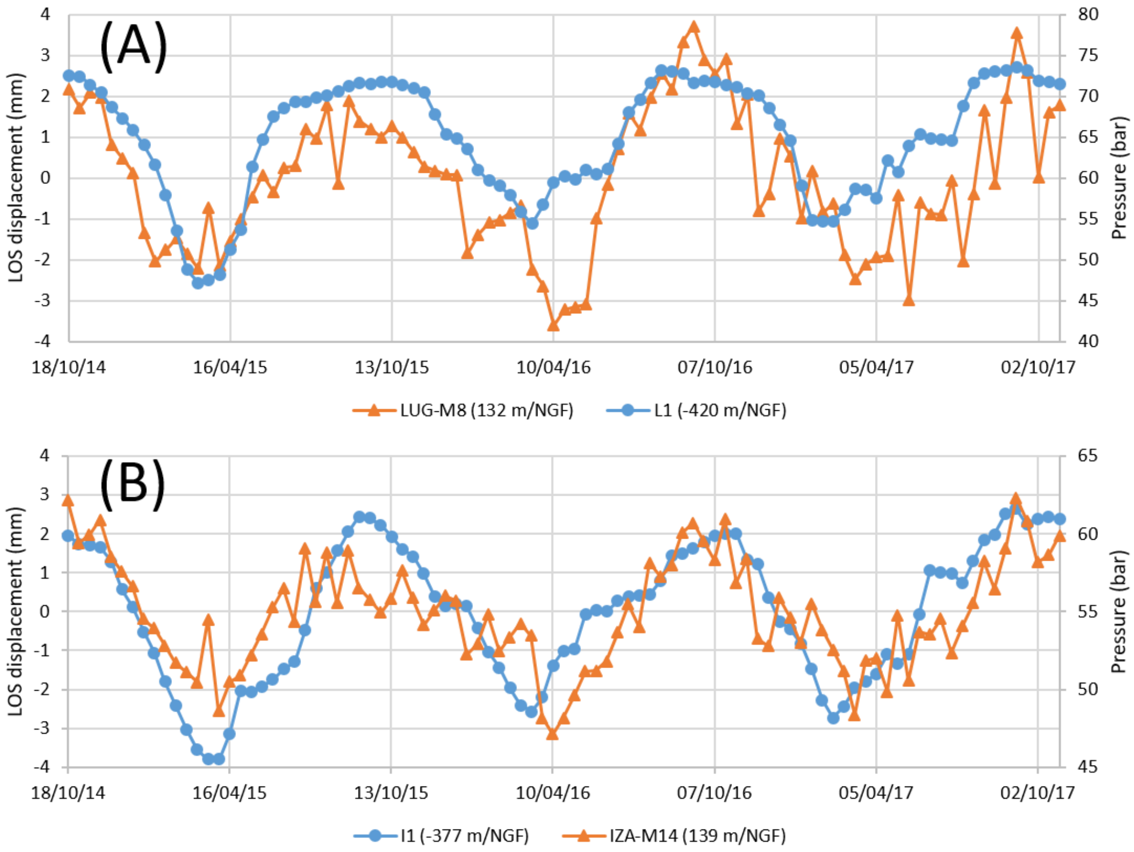

Figure 6: Comparison of average DInSAR Line of Sight (LOS) displacement and bottomhole pressure at both exploitation wells locations: (A) Lussagnet case, (B) Izaute case.

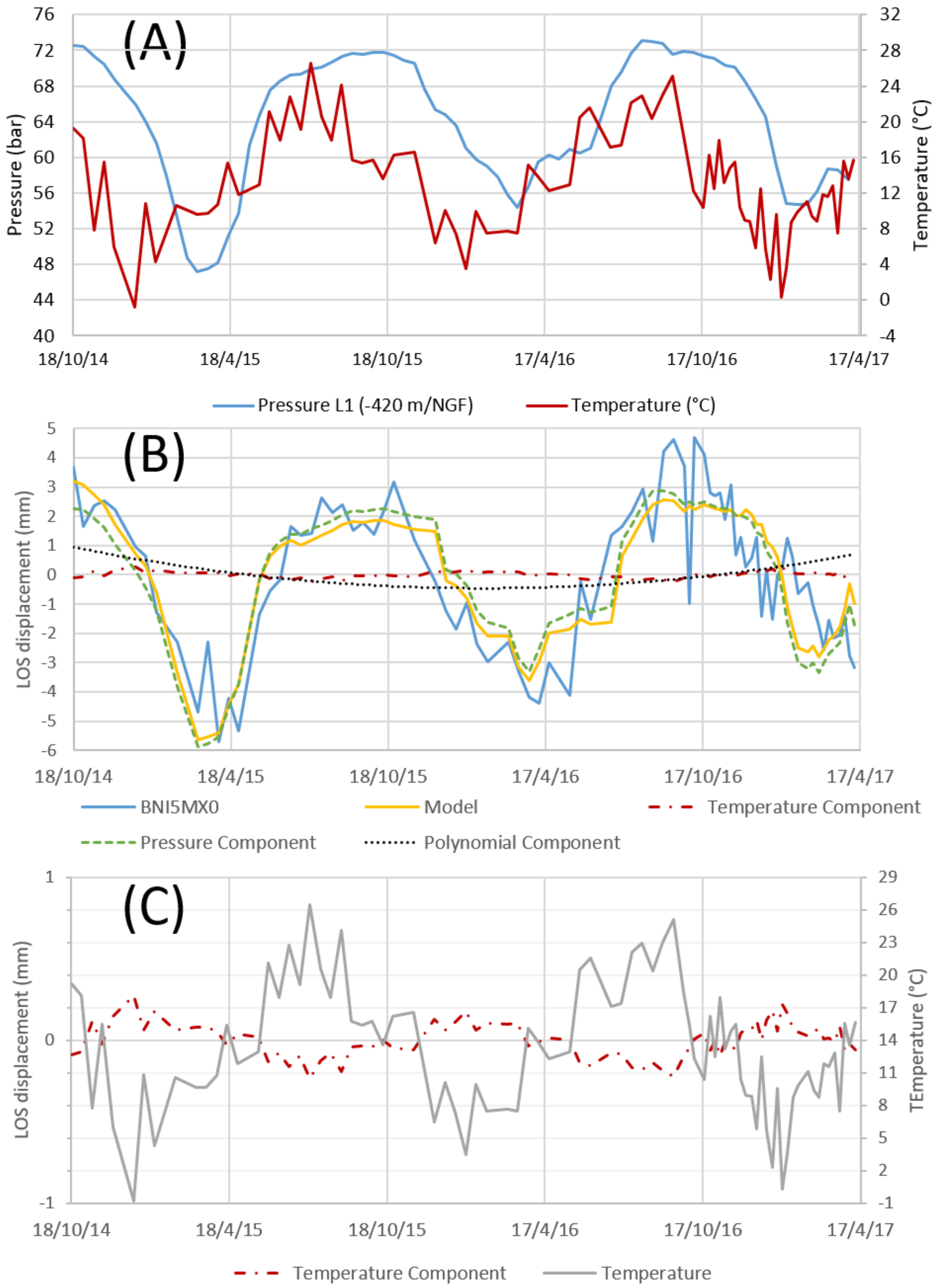

Figure 7: Additive decomposition of the LOS displacement at the Lussagnet site using the reservoir pressure and the surface temperature. (A) Time profiles of the temperature from Mont-de-Marsan weather station and the gas pressure at Lussagnet well L1 during 2.5 years. (B) Additive decomposition of the LOS displacement near L1 (BNI5MX0). (C) Comparison of the temperature component of the LOS displacement at BNI5MX0 and the surface temperature.

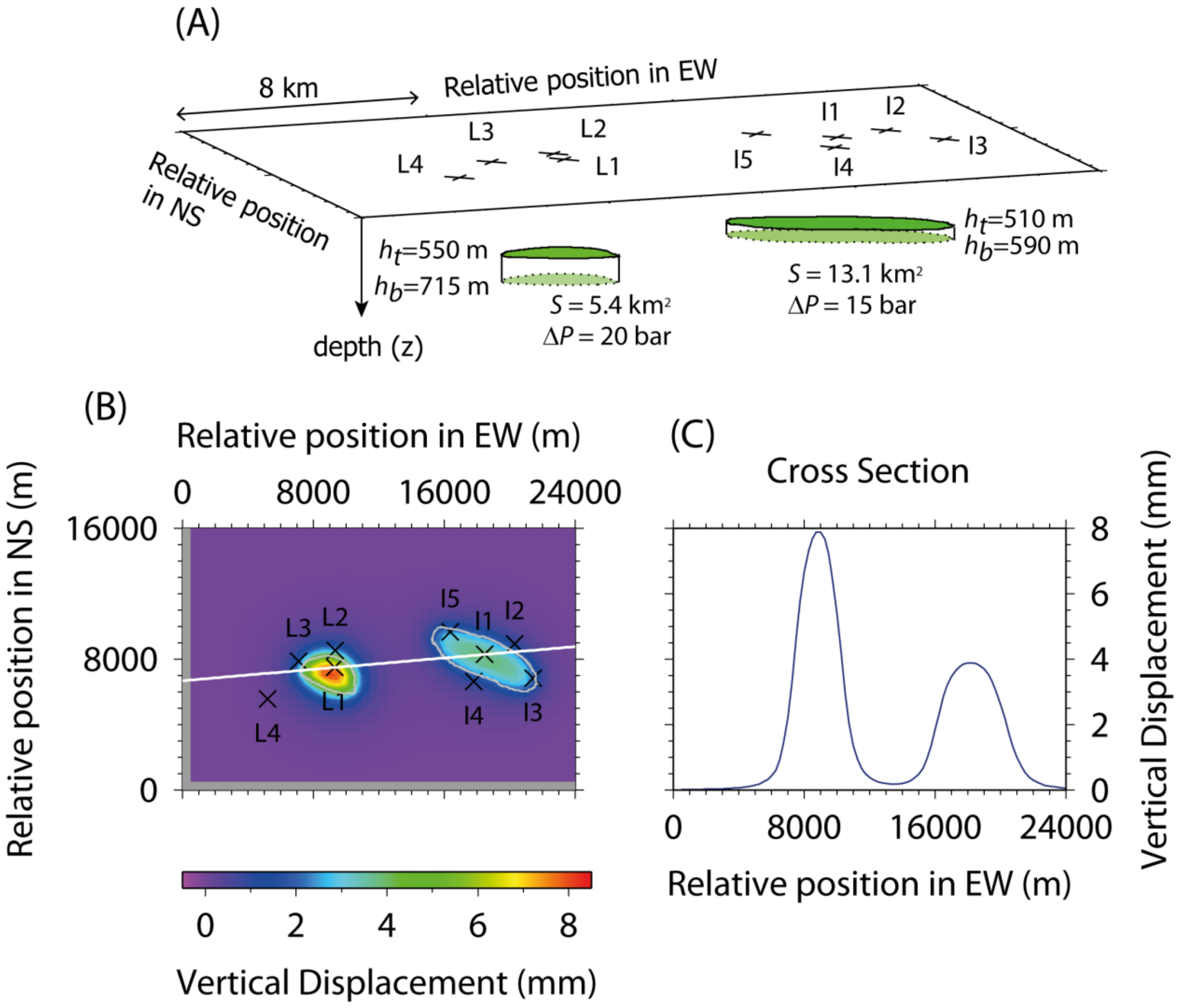

Figure 8: (A) Geometry of both reservoirs (in green) (surface S, top depth ht and bottom depth hb) and pressure variations ΔP used by the model. Also shown are the locations of the exploitation wells L1 and I1, the monitoring wells (L2, L3 and L4) and (I2, I3, I4, I5) at the Lussagnet and Izaute site, respectively. (B) Vertical displacements calculated by the model after the simultaneous gas injections at L1 and I1. (C) Cross section (white line on the left) gives the vertical displacement at L1 and I1 peaks.

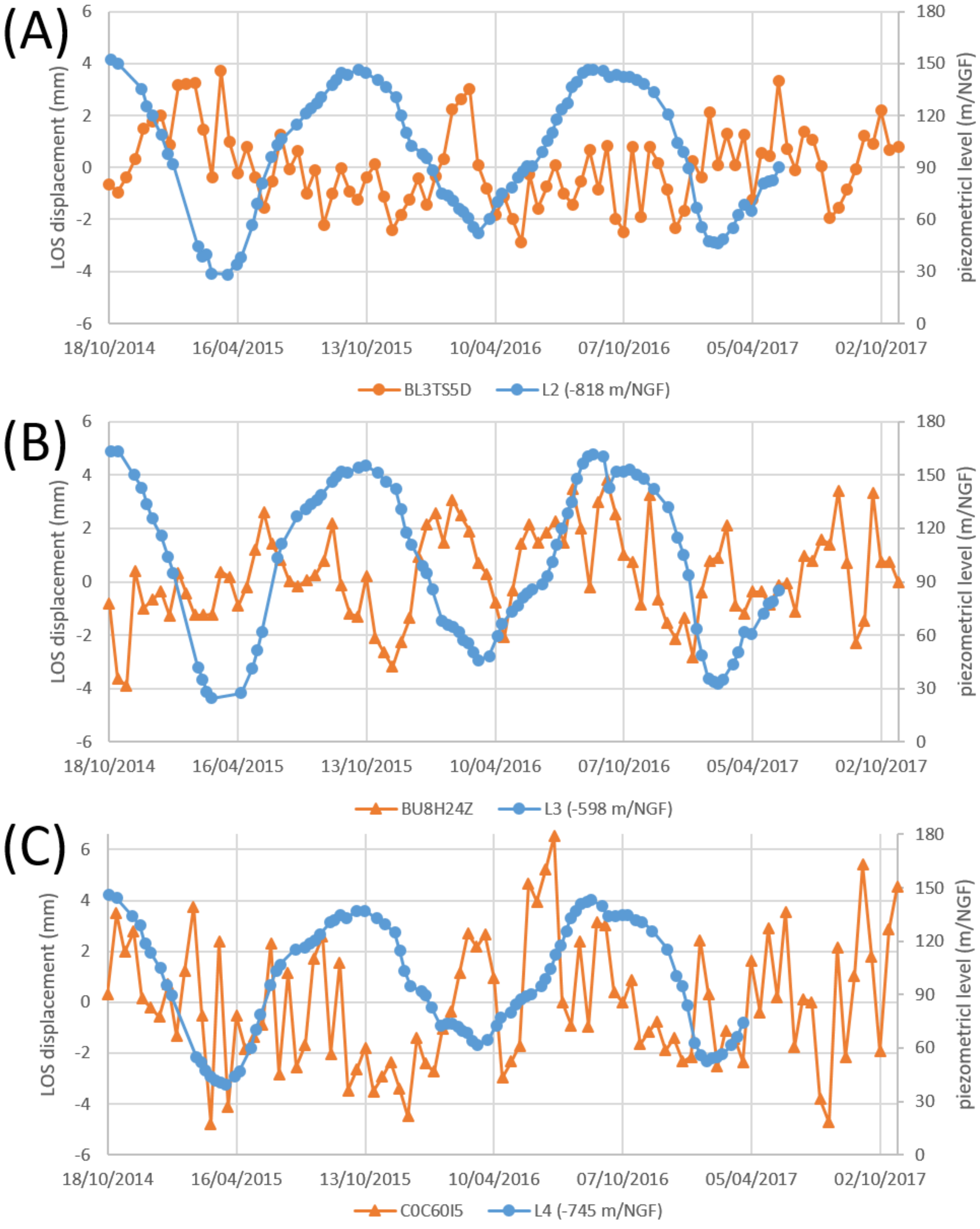

Figure 9: Comparison of LOS displacement and piezometric level at three Lussagnet monitoring wells locations: (A) L2, (B) L3, (C) L4.

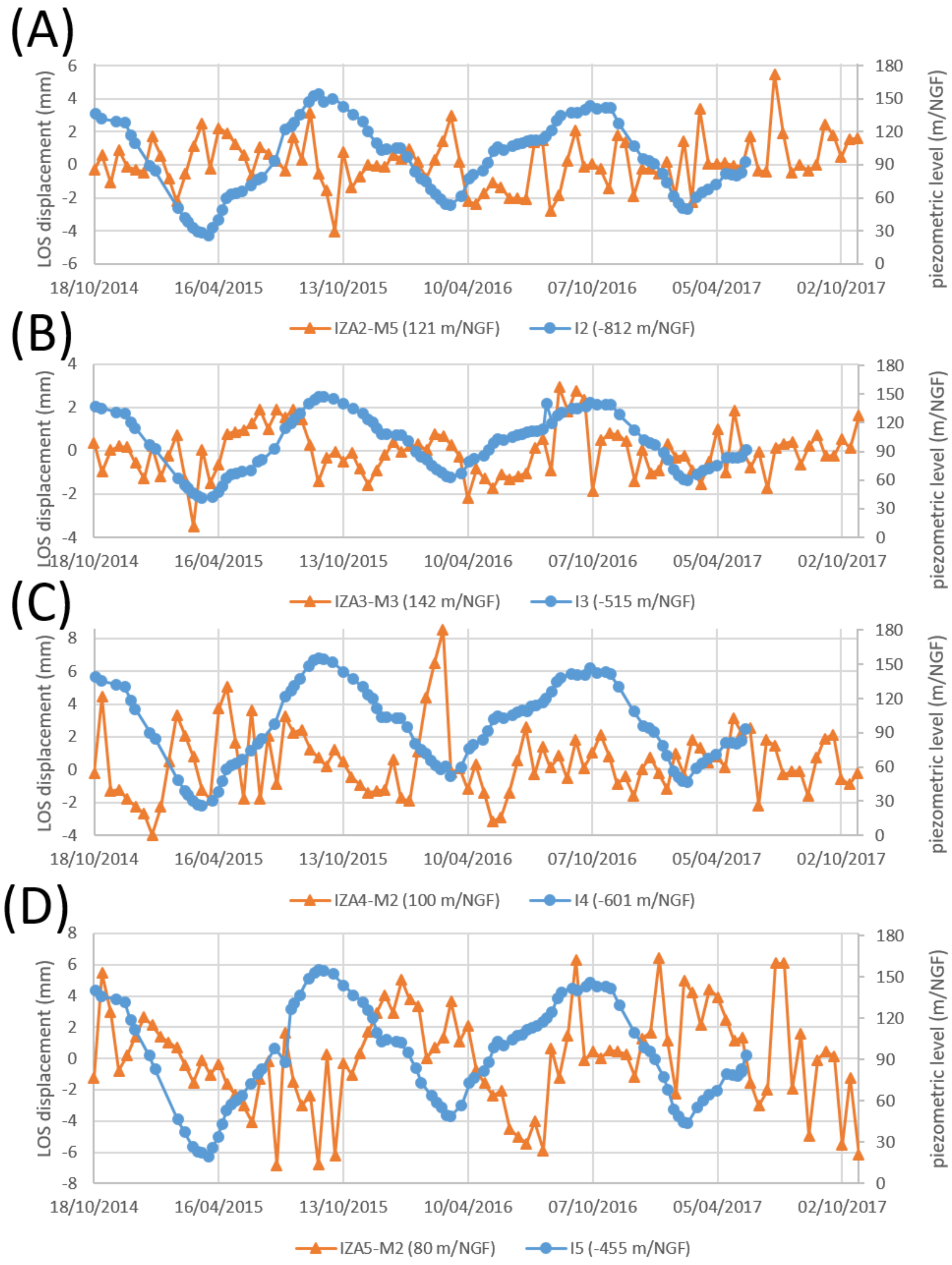

Figure 10: Comparison of mean LOS displacement and piezometric level at four Izaute monitoring wells locations: (A) I2, (B) I3, (C) I4, (D) I5.

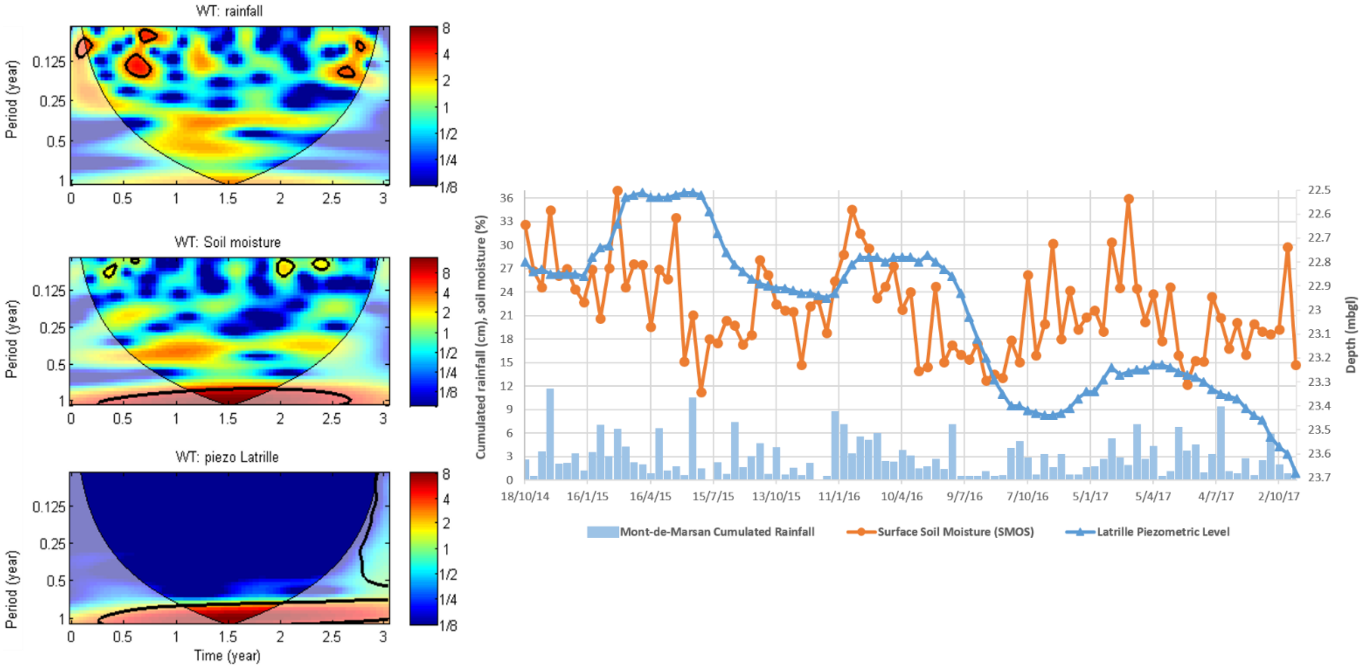

Figure 11: On the right, the comparison of the time series of these three potential triggering factors. On the left, the Continuous wavelet transform (CWT) of three potential triggering factors time series: (1) cumulated rainfall at Mont-de-Marsan Weather station, (2) surface soil moisture at the 25 km SMOS grid cell around the studied area, (3) Latrille piezometric level at Latrille. The thick contour designates the 5 % significant level against red noise. The cone of influence (COI) where edge effects might distort the picture is shown as a lighter shadow.

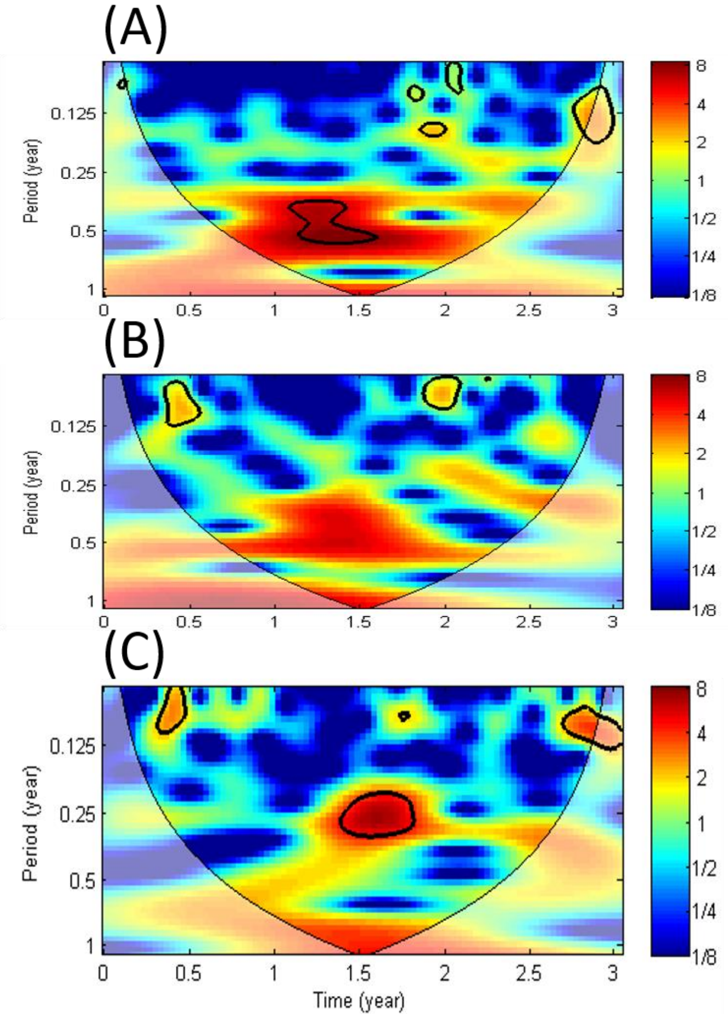

Figure 12: Continuous wavelet transform (CWT) of the mean LOS displacements in at three Lussagnet monitoring wells: (A) L3, (B) L2, (C) L4. The thick contour designates the 5 % significant level against red noise. The cone of influence (COI) where edge effects might distort the picture is shown as a lighter shadow.

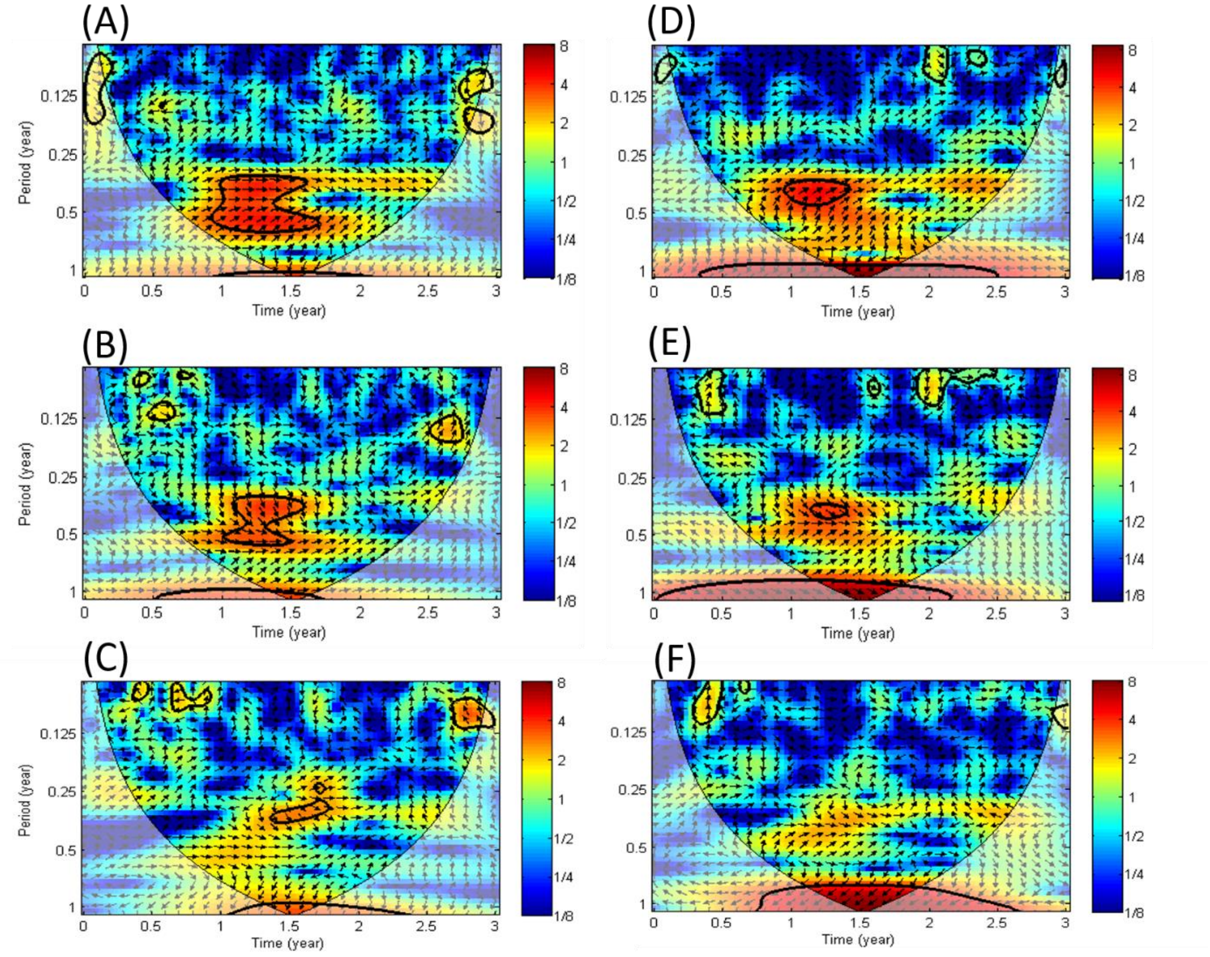

Figure 13: On the left, cross wavelet transform (XWT) of the cumulated rainfall and the LOS displacement at three Lussagnet monitoring wells: (A) L3, (B) L2, (C) L4. The relative phase relationship is shown as arrows, with in-phase pointing right and anti-phase pointing left and the rainfall leading by 90° pointing straight down. On the right, the same transforms are shown using the surface soil moisture (SSM) instead of the rainfall: (D) L3, (E) L2, (F) L4.

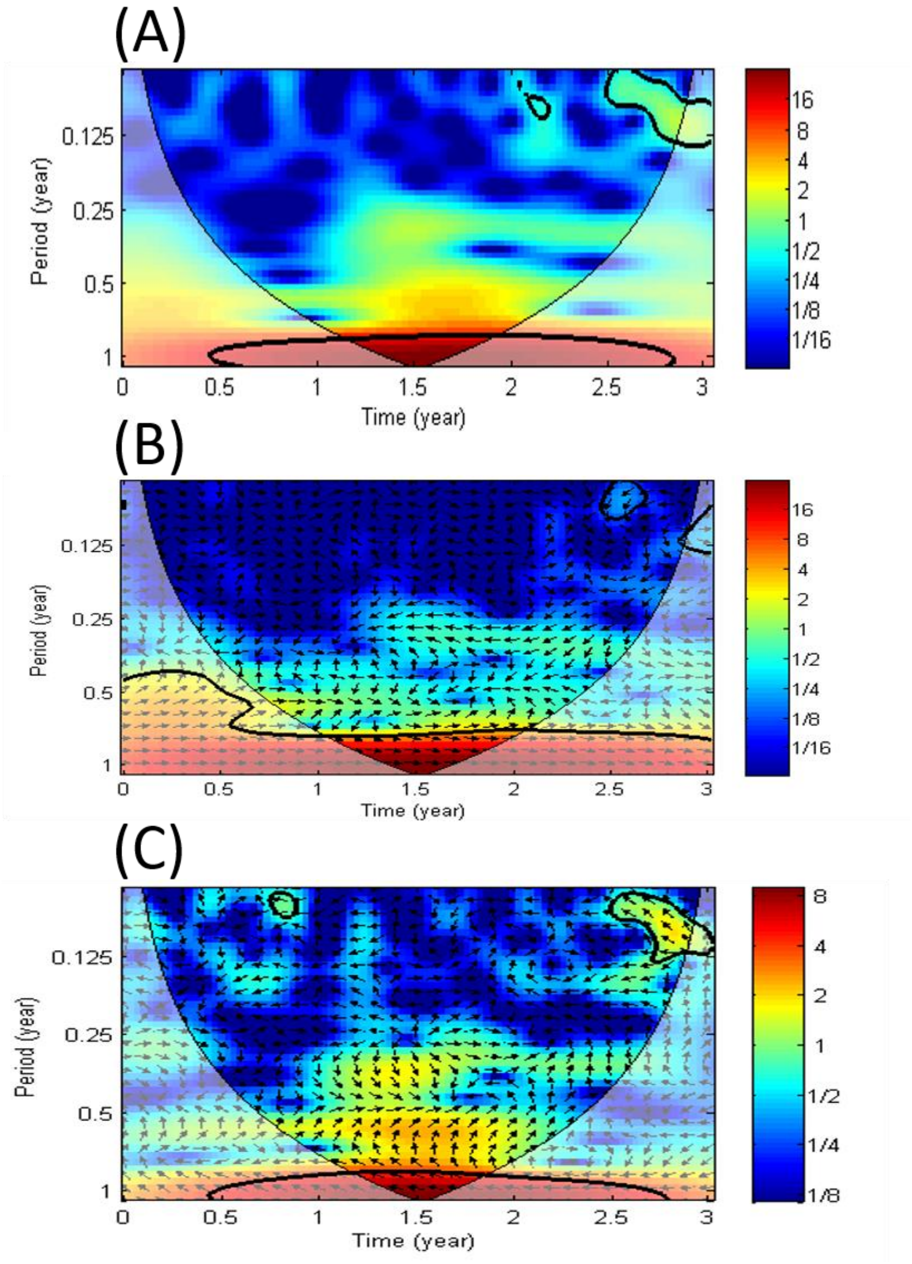

Figure 14: (A) Continuous wavelet transform (CWT) of the mean LOS displacement around the Lussagnet injection wells (LUG-M8). (B) Cross wavelet transform (XWT) of the pressure in the deep reservoir and LUG-M8. (C) Cross wavelet transform (XWT) of the cumulated rainfall and LUG-M8. The relative phase relationship is shown as arrows, with in-phase pointing right and anti-phase pointing left and the first time series leading by 90° pointing straight down.

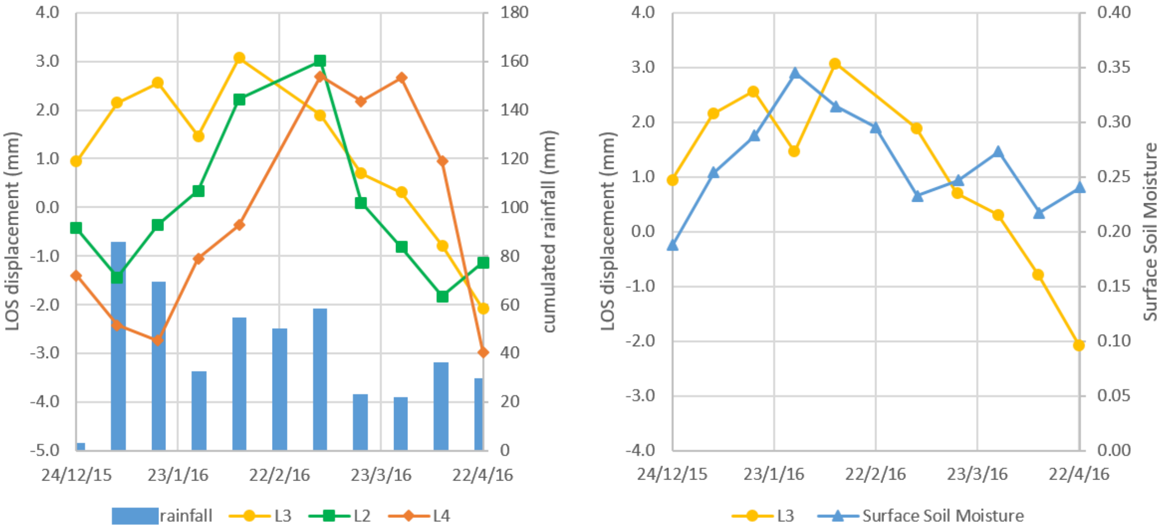

Figure 15: On the left, the comparison of LOS displacement at three Lussagnet monitoring wells locations (L3, L2 and L4) during the 6-month time period where the rainfall might influence the surface LOS displacement (see text). On the right, the surface soil moisture is compared to the LOS displacement at L3 during the same period.

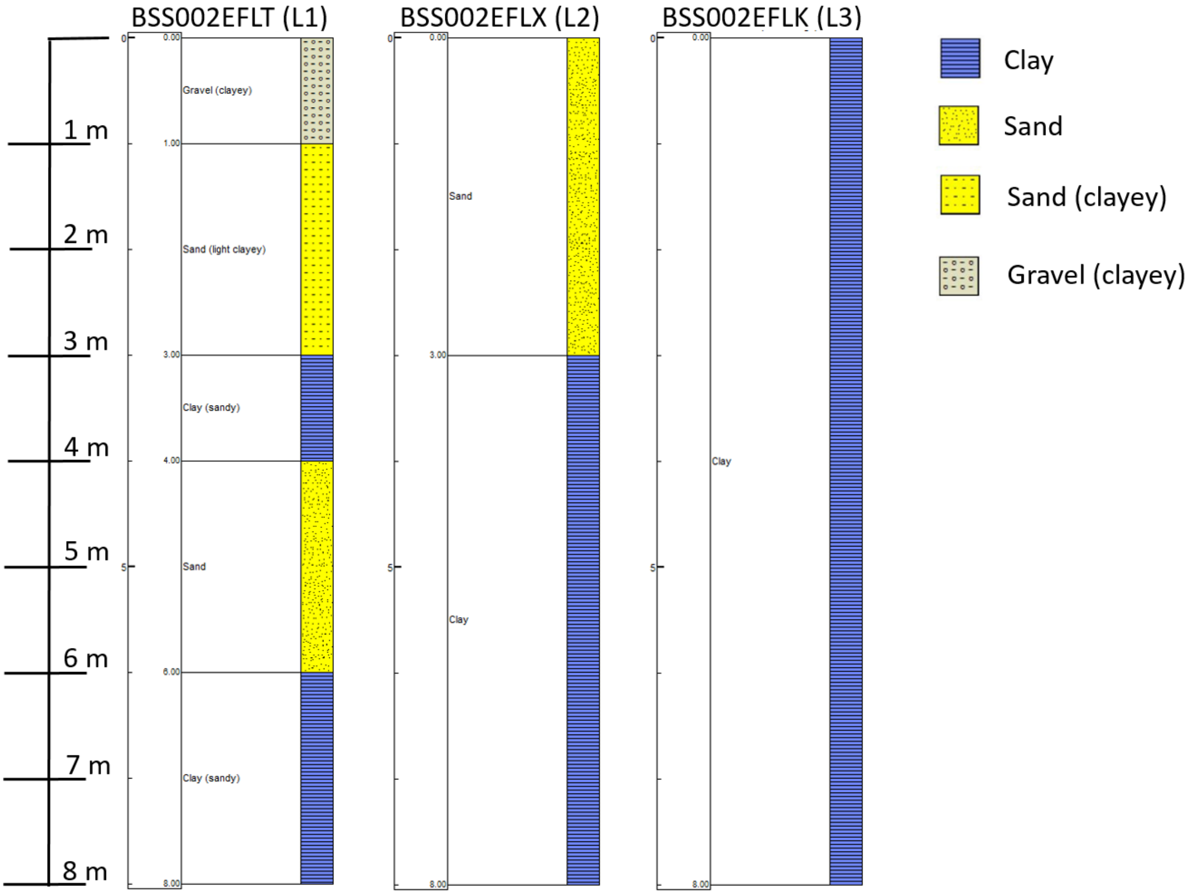

Figure 16: Geological Logs near the Lussagnet exploitation well (L1) and near two Lussagnet monitoring wells (L2, L3) extracted from the BRGM subsurface database ("Banque de données du sous-sol", http://infoterre.brgm.fr/).

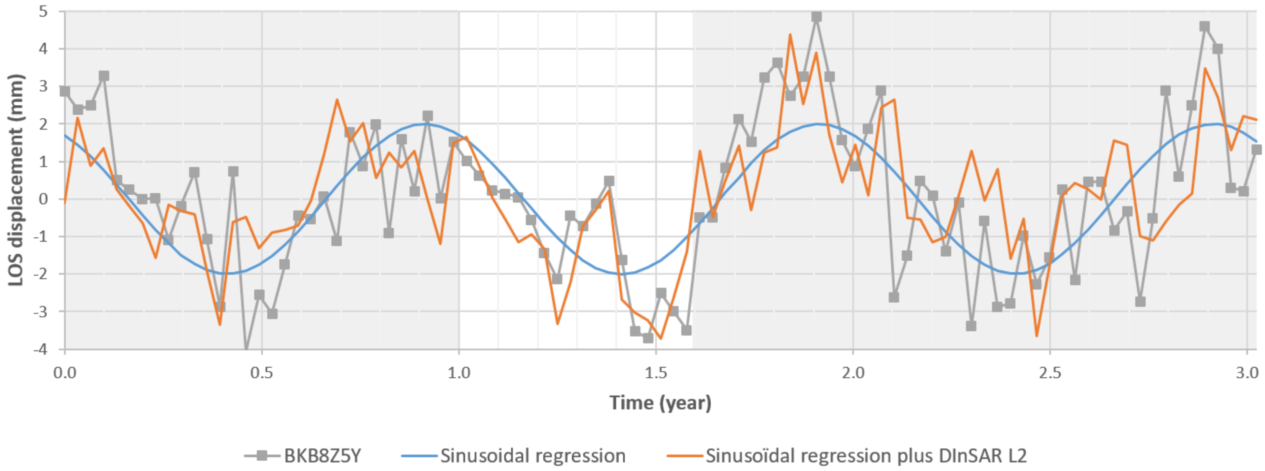

Figure 17: Modeling of LOS displacement at BKB8Z5Y location with the sinusoidal regression model and with the sum of the sinusoidal regression model and the DInSAR time series near L2 location. The 6-month time period where the rainfall might influence the surface LOS displacement (see text) is shown as a transparent window.

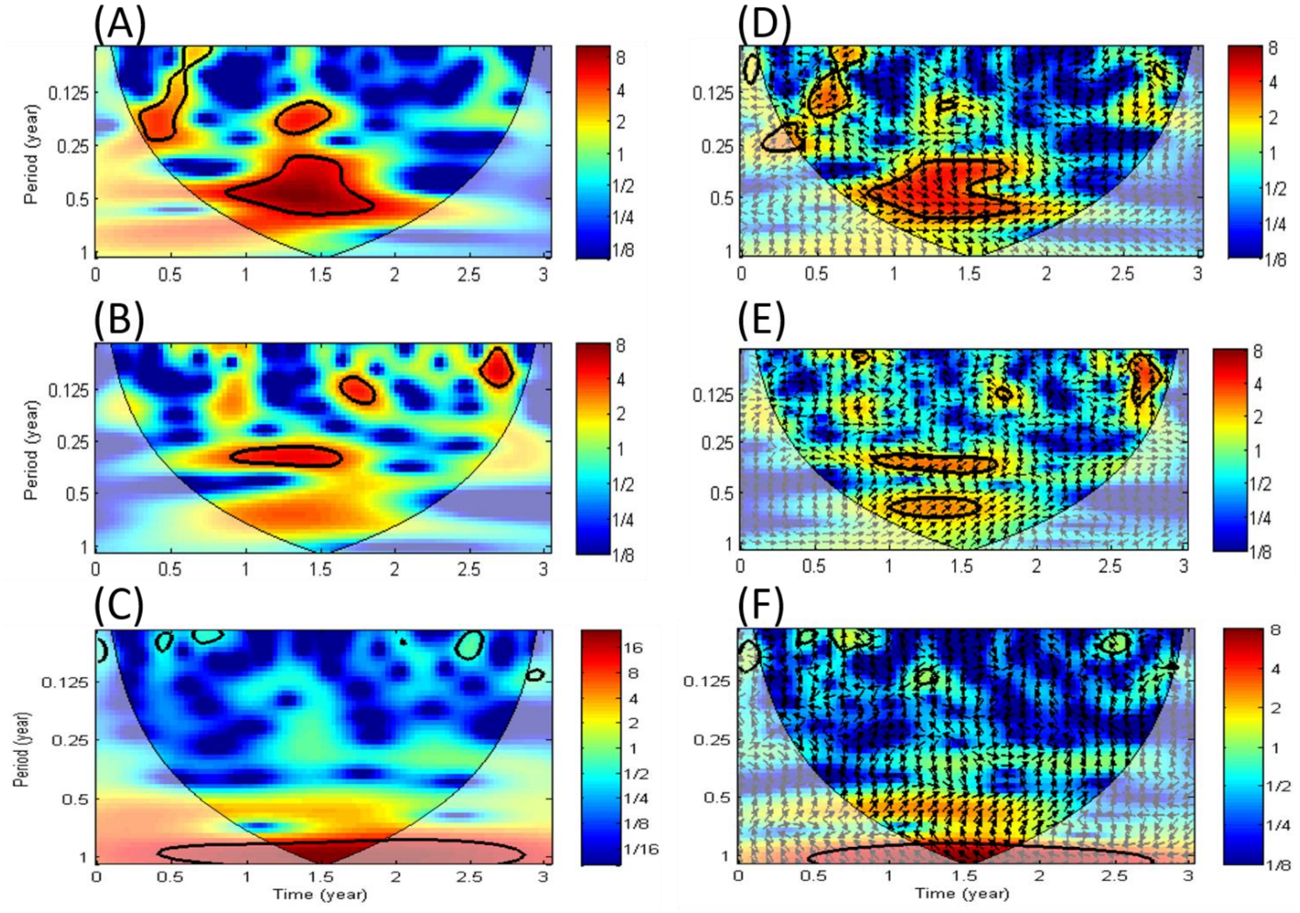

Figure 18: On the left, continuous wavelet transform (CWT) of the LOS displacements at three locations of the Izaute site: (A) I4, (B) I2, (C) I1. On the right, cross wavelet transform (XWT) of the cumulated rainfall and the LOS displacements are shown at these three locations: (A) I4, (B) I2, (C) I1. The relative phase relationship is shown as arrows, with in-phase pointing right and anti-phase pointing left and the rainfall leading by 90° pointing straight down.

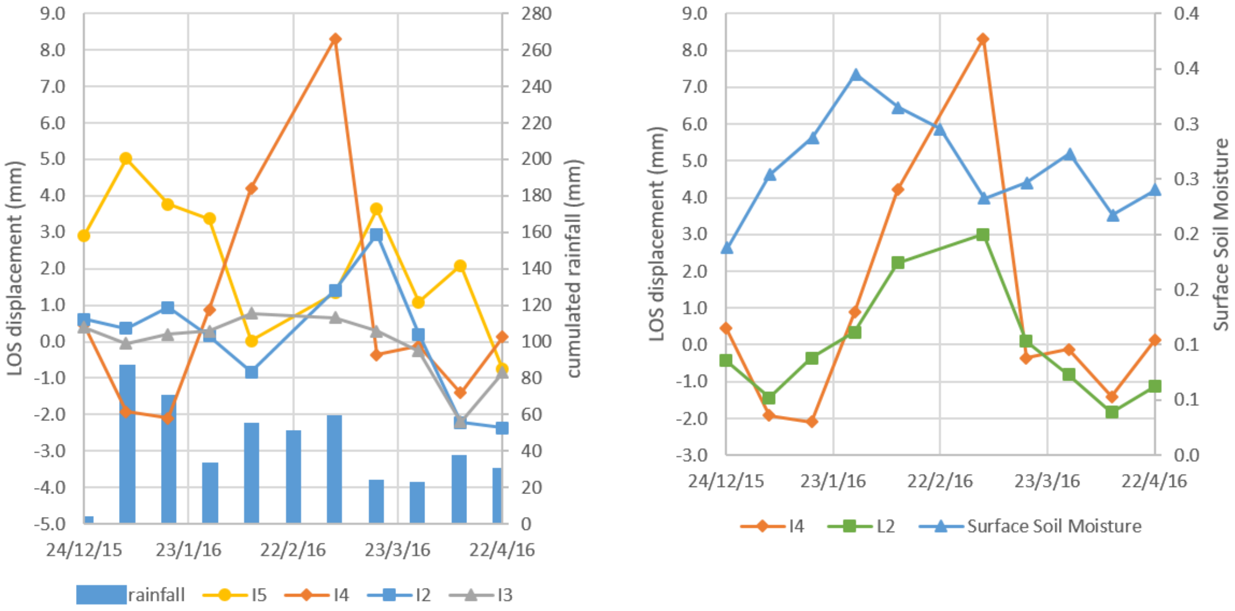

Figure 19: On the left, the comparison of LOS displacement at Izaute monitoring wells location (I5, I4, I2, I3) during the 6-month time period where the rainfall might influence the LOS displacement (see text). On the right, the Surface Soil Moisture and the LOS displacement at I4 is compared to the LOS displacement at L2 during the same period.

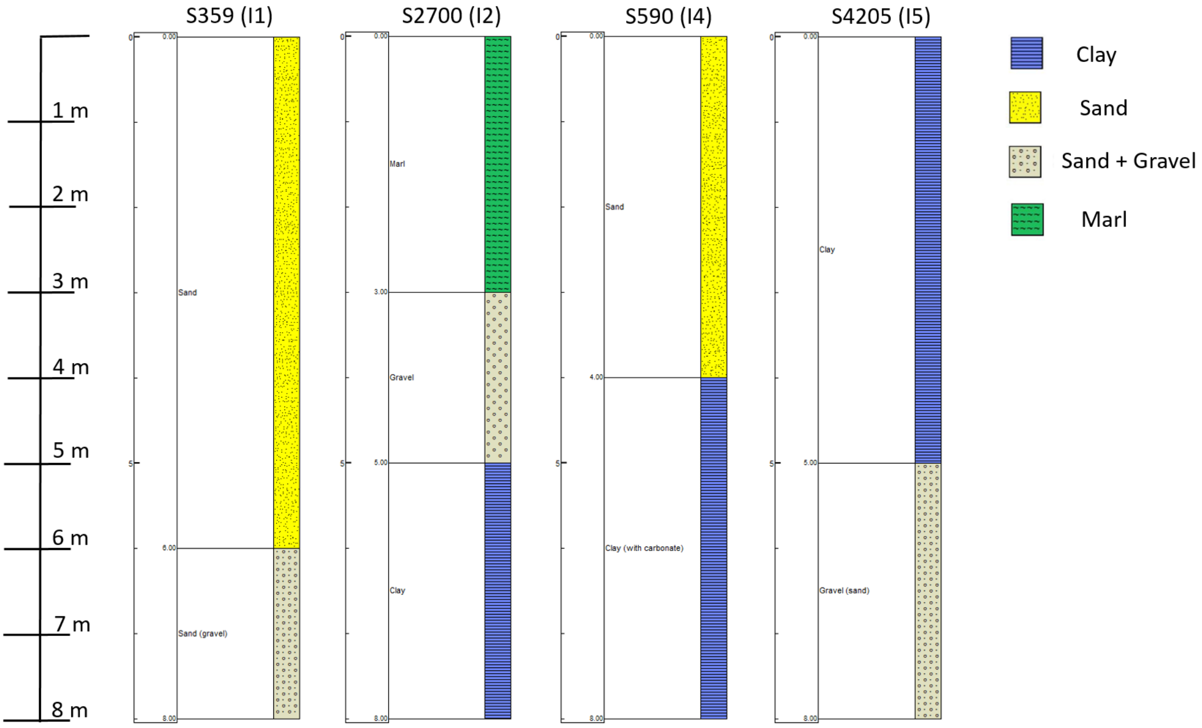

Figure 20: Geological Logs near the Izaute exploitation well (I1) and near three monitoring wells (I2, I4, I5) extracted from the BRGM subsurface database (“Banque de données du sous-sol”, http://infoterre.brgm.fr/).

Table 1: Model parameters used in the calculation of the vertical displacement

Parameter	**Quantity and Unit**
Poisson ratio ν	0.3
Medium rigidity μ	8 GPa
Biot's coefficient α	0.9
Geometry of Lussagnet reservoir (surface S, top depth h_t, bottom depth h_b)	(5.4 km^2, 550 m, 715 m)
pressure change ΔP in Lussagnet reservoir	20 bar
Geometry of Izaute reservoir (surface S, top depth h_t, bottom depth h_b)	(13.1 km^2, 510 m, 590 m)
pressure change ΔP in Izaute reservoir	15 bar